

## REPORT DOCUMENTATION PAGE

Form Approved OMB NO. 0704-0188

The public reporting burden for this collection of information is estimated to average 1 hour per response, including the time for reviewing instructions, searching existing data sources, gathering and maintaining the data needed, and completing and reviewing the collection of information. Send comments regarding this burden estimate or any other aspect of this collection of information, including suggestions for reducing this burden, to Washington Headquarters Services, Directorate for Information Operations and Reports, 1215 Jefferson Davis Highway, Suite 1204, Arlington VA, 22202-4302. Respondents should be aware that notwithstanding any other provision of law, no person shall be subject to any penalty for failing to comply with a collection of information if it does not display a currently valid OMB control number.

PLEASE DO NOT RETURN YOUR FORM TO THE ABOVE ADDRESS.

1. REPORT DATE (DD-MM-YYYY) 06-10-2010	2. REPORT TYPE MS Thesis	3. DATES COVERED (From - To) 2-Sep-2009 -		
4. TITLE AND SUBTITLE System performance of absolute quartz-crystal barometers with sub-microbar precision		5a. CONTRACT NUMBER W911NF-05-1-0398		
		5b. GRANT NUMBER		
		5c. PROGRAM ELEMENT NUMBER 611102		
6. AUTHORS Ganesh Kumar Subramanian		5d. PROJECT NUMBER		
		5e. TASK NUMBER		
		5f. WORK UNIT NUMBER		
7. PERFORMING ORGANIZATION NAMES AND ADDRESSES University of Massachusetts - Amherst Office of Grant & Contract Admin. 408 Goodell Building Amherst, MA 01003 -3285		8. PERFORMING ORGANIZATION REPORT NUMBER		
9. SPONSORING/MONITORING AGENCY NAME(S) AND ADDRESS(ES) U.S. Army Research Office P.O. Box 12211 Research Triangle Park, NC 27709-2211		10. SPONSOR/MONITOR'S ACRONYM(S) ARO		
		11. SPONSOR/MONITOR'S REPORT NUMBER(S) 49393-EV.4		
12. DISTRIBUTION AVAILABILITY STATEMENT Approved for Public Release; Distribution Unlimited				
13. SUPPLEMENTARY NOTES The views, opinions and/or findings contained in this report are those of the author(s) and should not be construed as an official Department of the Army position, policy or decision, unless so designated by other documentation.				
14. ABSTRACT The performance of absolute quartz-crystal barometers is analyzed and discussed. Their ability to measure sub-microbar, atmospheric pressure fluctuations at time scales down to seconds is demonstrated. The first observations of ocean-generated, atmospheric infrasound with periods of about 5 s and sub-microbar amplitudes, called microbaroms, using single absolute barometers are presented. It is concluded that these absolute quartz-crystal barometers can be used effectively for infrasound monitoring.				
15. SUBJECT TERMS air pressure, barometers, infrasound				
16. SECURITY CLASSIFICATION OF: a. REPORT UU		17. LIMITATION OF ABSTRACT UU	15. NUMBER OF PAGES	19a. NAME OF RESPONSIBLE PERSON Andreas Muschinski
				19b. TELEPHONE NUMBER 413-577-0898

## **Report Title**

System performance of absolute quartz-crystal barometers with sub-microbar precision

## **ABSTRACT**

The performance of absolute quartz-crystal barometers is analyzed and discussed. Their ability to measure sub-microbar, atmospheric pressure fluctuations at time scales down to seconds is demonstrated. The first observations of ocean-generated, atmospheric infrasound with periods of about 5 s and sub-microbar amplitudes, called microbaroms, using single absolute barometers are presented. It is concluded that these absolute quartz-crystal barometers can be used effectively for infrasound monitoring.



**SYSTEM PERFORMANCE OF ABSOLUTE  
QUARTZ-CRYSTAL BAROMETERS WITH  
SUB-MICROBAR PRECISION**

A Thesis Presented

by

GANESH KUMAR SUBRAMANIAN ANANTHANARAYANAN

Submitted to the Graduate School of the  
University of Massachusetts Amherst in partial fulfillment  
of the requirements for the degree of

MASTER OF SCIENCE

September 2009

Electrical and Computer Engineering

© Copyright by Ganesh Kumar Subramanian Ananthanarayanan 2009

All Rights Reserved

**SYSTEM PERFORMANCE OF ABSOLUTE  
QUARTZ-CRYSTAL BAROMETERS WITH  
SUB-MICROBAR PRECISION**

A Thesis Presented  
by  
GANESH KUMAR SUBRAMANIAN ANANTHANARAYANAN

Approved as to style and content by:

---

Andreas Muschinski, Chair

---

Patrick A. Kelly, Member

---

Douglas P. Looze, Member

---

Christopher V.Hollot, Department Chair  
Electrical and Computer Engineering

To my parents, Premlata and Ananthanarayanan.

## ACKNOWLEDGMENTS

I express my sincere gratitude to my advisor, Prof. Andreas Muschinski, for the encouragement and guidance he provided throughout my thesis while giving me the freedom to work in my own way. I am also grateful to the committee members, Prof. Patrick Kelly and Prof. Douglas Looze, for having accepted to be in my thesis committee and for their support and invaluable feedback. I would also like to thank my colleagues, Vincent Hohreiter and Alexander de Geofroy, who helped me with the data collection. I am thankful to Mr. Jerome Paros for donating the barometers that were used in my thesis.

My deepest gratitude goes to my uncle, Ramani Chidambaram, and aunt, Nithya Krishnan, for their constant source of support during my graduate studies. Finally, I would like to thank my friends Harsha Sriramagiri, Sudarshan Narayanan, Pritish Narayanan, Kamlesh Vasudevan, Ashwin Bhaskar, Vijey Balaji, Arun Srinivasan, Avanidhar Chandrasekaran and my brother Prasshanth for their assistance and moral support throughout my thesis.

The material presented in this thesis is based on work supported in part by the U.S. Army Research Laboratory and the U.S. Army Research Office under grant 49393-EV, by the National Science Foundation under grant ATM-0444688, and by the Jerome M. Paros Endowment in Measurement Sciences.

## **ABSTRACT**

# **SYSTEM PERFORMANCE OF ABSOLUTE QUARTZ-CRYSTAL BAROMETERS WITH SUB-MICROBAR PRECISION**

SEPTEMBER 2009

GANESH KUMAR SUBRAMANIAN ANANTHANARAYANAN

B.E., ANNA UNIVERSITY, CHENNAI, INDIA

M.S., UNIVERSITY OF MASSACHUSETTS AMHERST

Directed by: Professor Andreas Muschinski

In this thesis, the performance of absolute quartz-crystal barometers is presented, and their ability to measure, with sub-microbar precision, atmospheric pressure fluctuations with periods as short as a few seconds is demonstrated. The first observations of ocean-generated atmospheric infrasound with periods of about 5 s and sub-microbar amplitudes, called microbaroms, using single absolute barometers are presented. These barometers can measure microbaroms with amplitudes down to 50 nanobars and the 1-h estimates of microbarom amplitudes calculated from data collected independently with three collocated barometers differed by only a few nanobars. The uncorrelated noise spectral density during calm weather conditions is about  $10^{-4}$  Pa<sup>2</sup>/Hz. The observed microbaroms have amplitudes between 0.2  $\mu$ bar and 1  $\mu$ bar with periods between 3 s and 8 s. The relative accuracy between the barometers is of the order of a few pascals. It is concluded that these absolute quartz-crystal barometers can be used effectively for infrasound monitoring.

## TABLE OF CONTENTS

	Page
<b>ACKNOWLEDGMENTS .....</b>	<b>v</b>
<b>ABSTRACT .....</b>	<b>vi</b>
<b>LIST OF TABLES .....</b>	<b>ix</b>
<b>LIST OF FIGURES.....</b>	<b>x</b>
 <b>CHAPTER</b>	
<b>1. INTRODUCTION .....</b>	<b>1</b>
<b>2. ATMOSPHERIC WAVES .....</b>	<b>4</b>
2.1 Gravity Waves .....	4
2.2 Infrasound Waves.....	5
2.3 Atmospheric Tides.....	5
2.4 Atmospheric Seiches .....	6
<b>3. EXPERIMENT .....</b>	<b>7</b>
3.1 Instruments and Data Acquisition .....	7
3.1.1 Quartz Crystal Barometers .....	7
3.1.2 Ultrasonic Anemometers .....	11
3.1.3 Data Logger .....	13
3.2 Experiment Setup and Timeline .....	14
<b>4. DATA PROCESSING .....</b>	<b>22</b>
4.1 Converting ASCII Data Files to MAT Files .....	22
4.2 Block Averaging to Obtain Equidistant Time Stamps.....	25
4.3 Discrete Time Filtering.....	27

4.3.1	Design of Discrete-Time FIR Bandpass Filter . . . . .	28
4.3.2	Filtering using Discrete-Time FIR Filter . . . . .	32
4.4	Power Density Spectrum and Coherence Function . . . . .	36
4.4.1	Estimation of the Power Spectrum of Random Signals . . . . .	37
4.4.2	Welch's Method: Averaging Modified Periodogram . . . . .	38
4.5	Computation of Microbarom Amplitude and Frequency . . . . .	43
4.6	Spectrogram . . . . .	45
<b>5.</b>	<b>RESULTS AND INTERPRETATION . . . . .</b>	<b>47</b>
5.1	First Observations of Microbaroms using Single Absolute Barometers . . . . .	47
5.2	Temporal Variations of the Amplitude and Frequency of the Microbaroms . . . . .	58
5.3	Performance of the Barometers and the DigiPort . . . . .	66
<b>6.</b>	<b>CONCLUSIONS AND DISCUSSIONS . . . . .</b>	<b>76</b>
<b>BIBLIOGRAPHY . . . . .</b>		<b>79</b>

## LIST OF TABLES

<b>Table</b>	<b>Page</b>
3.1 Timeline of operation of the sensors, along with their settings .....	21
4.1 Barometer data output format .....	23
4.2 Block averaged time stamps on 06 Mar, 2008 .....	27
4.3 Parameters of the FIR bandpass filter for the microbaroms .....	33

## LIST OF FIGURES

<b>Figure</b>	<b>Page</b>
3.1 Data Logger in its protective enclosure by Campbell Scientific .....	15
3.2 Graphical representation of the operational timeline of the sensors .....	17
3.3 Photograph of the barometers with data dogger inside the travel trailer .....	19
3.4 Photograph of the travel trailer and the anemometer .....	20
4.1 Pressure time series during a 24 h period .....	24
4.2 The averaged and non-averaged pressure data .....	27
4.3 Rectangular and Blackman windows in the time domain .....	34
4.4 Magnitude response of the rectangular and Blackman windows .....	35
4.5 Frequency response of the bandpass filter for the microbaroms .....	36
5.1 Raw pressure time series over a 2-hr time interval .....	48
5.2 Time series of the difference between the three signals of figure 5.1 .....	49
5.3 Power spectral density of the data in figure 5.1 .....	50
5.4 Bandpass filtered time series of data in figure 5.1 for barometer #103946 .....	51
5.5 The data within the 3-min long time window indicated by the rectangle in figure 5.1 .....	52
5.6 Power spectral density of the data in figure 5.5 .....	54
5.7 Bandpass filtered time series of data in figure 5.5 .....	54

5.8	Time series of the difference between the three signals of figure 5.5 . . . . .	55
5.9	Raw pressure time series between 1900 EST on 14 Mar and 1900 EST on 20 Mar 2008 . . . . .	56
5.10	Spectrogram of data in figure 5.9 . . . . .	57
5.11	Horizontal wind speed time series between 1900 EST on 14 Mar and 1900 EST on 20 Mar 2008 . . . . .	57
5.12	Raw pressure time series between 26 Feb and 11 Mar 2008 . . . . .	59
5.13	Spectrogram of data in figure 5.12 with the centroid frequency . . . . .	59
5.14	Horizontal wind speed time series between 1900 EST on 25 Feb and 1900 EST on 11 Mar 2008 . . . . .	60
5.15	Zoomed-in segment of figures 5.13 and 5.14 between 06 Mar and 09 Mar 2008 . . . . .	60
5.16	Microbarom amplitude time series of data in figure 5.12 . . . . .	62
5.17	Zoomed-in version of the spectrogram in figure 5.12 . . . . .	62
5.18	Zoomed-in version of microbarom amplitude time series of figure 5.16 . . . . .	63
5.19	Power spectral density of barometer #103946 between 1430 and 1500 EST on 06 Mar 2008 . . . . .	65
5.20	Power spectral density of barometer #103946 between 0000 and 0030 EST on 07 Mar 2008 . . . . .	65
5.21	Time series of the difference between the three signals between 1900 EST on 15 Mar, 2008 and 1900 EST on 19 Mar, 2008 . . . . .	66
5.22	Horizontal wind speed and temperature time series between 1900 EST on 15 Mar, 2008 and 1900 EST on 19 Mar, 2008 . . . . .	67
5.23	Time series of figure 5.21 shown in three separate subplots . . . . .	67
5.24	Power spectral density between 0400 and 0600 EST on 18 Mar 2008 . . . . .	69

5.25 Power spectral density between 1200 and 1400 EST on 17 Mar 2008 .....	70
5.26 Spectrogram of the signals measured by the three barometers between 1900 EST on 14 Mar, 2008 and 1900 EST on 20 Mar, 2008 .....	73
5.27 Coherence spectrogram between the signals measured by the three barometers between 1900 EST on 14 Mar, 2008 and 1900 EST on 20 Mar, 2008.....	74

# CHAPTER 1

## INTRODUCTION

Microbaroms are atmospheric infrasound waves first observed by Benioff and Gutenberg (1939) using an electromagnetic microbarograph at the California Institute of Technology [5][6]. Microbaroms are generated by the nonlinear interaction of ocean surface waves, with similar frequencies, traveling in nearly opposite directions [1][24] and have a frequency twice as that of the ocean surface waves generating them. Earlier studies confirm that such sources of microbaroms are related to the high seas and regions of marine storms [11][10][9][8]. Microbaroms propagate through atmospheric waveguides that are governed by the wind and temperature structure of the atmosphere [12]. Donn and Rind (1972) showed that the variations in amplitude and frequency of the microbaroms observed at a ground based station are related to the propagation path and hence, the wind and temperature structure of the atmosphere. The measurement of microbaroms has been shown to be a useful and relatively inexpensive method of remotely sensing the thermal and wind structure of the upper atmosphere [12]. Nowadays, microbaroms have been observed using highly sensitive microphone arrays [31]. The temporal change in the arrival azimuth of microbaroms, determined using an infrasound measurement array, could be used as a method to track the movement of hurricanes [16].

An absolute barometer is an instrument that measures atmospheric pressure. Nowadays, highly sensitive barometers, called microbarometers, are used to measure air pressure fluctuations with high precision. Microbarometers, as the name

suggests, typically have a resolution of microbars ( $\mu$ bar), while ordinary barometers have a resolution of hectopascals (hPa) or millibars (mbar). An important purpose of microbarometers used around the world, is to monitor compliance with the Comprehensive Nuclear-Test-Ban Treaty by detecting the infrasound signature of a nuclear explosion, which can propagate for long distances. Such highly sensitive microbarometers could be used to detect microbaroms, observed as pressure fluctuations of few microbars ( $\mu$ bar) [12]. The only reported case of microbarom observation using absolute barometers is presented in [20]. Their setup had comprised of a cross array of 28 barometers (Model 216B-250 manufactured by Paroscientific, Inc.) in central Honshu, Japan. To detect microbaroms, they had used array processing techniques by computing the cross-spectral densities between every pair of barometers.

In this thesis, the primary focus has been on the capability of absolute quartz-crystal barometers (Intelligent Transmitters Series 6000, manufactured by Paroscientific, Inc.) to detect microbaroms individually as opposed to detection by an array (as in[20]). The barometers that have been concentrated in this thesis and the barometers that were used in [20] have been manufactured by the same manufacturer (Paroscientific, Inc.). Three quartz-crystal barometers of the type mentioned above were used to measure pressure for about six months with the settings of at least one barometer being different from the other two. Such different settings were used in order to determine the best setting for the detection of microbaroms. The significance of the digiport, a device (when connected to these barometers) that reduces wind induced pressure fluctuations, has been analyzed with respect to the detection of microbaroms. The relative accuracy between the barometers and the lowest detectable amplitude have been estimated quantitatively which are very important to evaluate the effectiveness of these barometers in an infrasound array. Also, attempt has been made to relate the temporal changes in amplitude and frequency of the observed microbaroms

to the lower tropospheric winds.

This thesis is organized in the form of six chapters including this chapter. Some atmospheric waves that are observed as pressure fluctuations are described in Chapter 2. Chapter 3 describes in detail about the sensors used and the experimental setup. Also listed in the chapter, are the important events during the experiment in chronological order, and finally the timeline of operation of the sensors is presented. In Chapter 4, all the data processing techniques used to analyze the data have been explained. The first couple of sections include the techniques that get the data ready for actual data analysis. Sections 4.3 to 4.6 explain the other data analysis techniques used. In Chapter 5, the results are presented and interpreted as clearly as possible. In the last chapter, the conclusions and discussions are presented.

# **CHAPTER 2**

## **ATMOSPHERIC WAVES**

Atmospheric waves are characterized as periodic disturbances in atmospheric variables like temperature, wind and air pressure. Such atmospheric waves that propagate are called traveling waves while those that do not propagate are called stationary waves. In this chapter, some atmospheric waves that are observed as pressure fluctuations will be described.

### **2.1 Gravity Waves**

Gravity waves are waves generated inside a fluid medium or at the interface between two media due to the interactions between the fluids at the interface with the restoring force being the force of gravity. Gravity waves at the ocean-air interface are called surface gravity waves. When the equilibrium of an ocean-air interface is disturbed, oscillations of the fluid parcels occur about the equilibrium position. These oscillations have typical periods ranging from 1 s to 30 s. Gravity waves within a fluid medium are called internal waves. Internal gravity waves generally have higher amplitudes and lower frequencies than surface gravity waves. Typically internal gravity waves in the atmosphere have periods between a few minutes and about one hour and amplitudes between a few pascals and a few hectopascals (hPa) [14] [22].

## 2.2 Infrasound Waves

Infrasound waves are sound waves whose frequency is between 0.01 Hz and 20 Hz. Infrasound waves generally travel longer distances with little dissipation in their energy. There are many sources of infrasound like naturally occurring phenomena (earthquakes, volcanic eruptions, surf [13], air flow over mountains, etc.)[3], mechanical machines (wind-turbines), and animals (elephants, whales). Each source has its characteristic frequency. The Comprehensive Nuclear-Test-Ban Treaty Organization uses infrasound to monitor compliance with the treaty.

Infrasonic waves generated by ocean surface waves are known as microbaroms [1][10][9]. These waves were first observed by Benioff and Gutenberg (1939) using an electromagnetic microbarograph at the California Institute of Technology [5][6]. They have frequencies between 0.15 Hz and 0.3 Hz and their amplitudes range from a few hundred nanobars to a few microbars [12][31]. Infrasound waves generated by wind flow over mountainous regions (mountain-generated infrasound) have periods greater than 20 s. High winds and local turbulent wind eddies obscure the underlying infrasound.

## 2.3 Atmospheric Tides

Atmospheric tides are oscillations of the atmospheric pressure caused by: 1) the solar heating of the atmosphere, 2) the moon's and the sun's gravitational attraction on the atmosphere and 3) the ocean tides.

The periodic heating of the earth's atmosphere by solar radiation gives rise to the generation of atmospheric tides. The atmosphere gets heated by the sun only during the day and not during the night: atmospheric tides are created due to this diurnal

cycle of heating the earth's atmosphere. These thermally generated tides have the largest magnitude amongst the atmospheric tides due to other sources. Thermally generated atmospheric tides have periods of 24 h (solar day), called the solar diurnal period. Periods of 12 h (semidiurnal), 8 h and 6 h can also be seen with relatively smaller amplitudes - these can be attributed to the harmonics generated by the solar heating pattern.

Lunar atmospheric tides are caused by the gravitational effects of the moon on the earth's atmosphere. Lunar tides also have the diurnal and semidiurnal components. Lunar diurnal tidal period is about 24.8 h (lunar day), while the lunar semidiurnal period is 12.4 h [15].

## 2.4 Atmospheric Seiches

Atmospheric seiches are analogous to the sloshing motion of water that occurs in lakes due to one or more disturbances. These seiches can be thought of as standing waves (formed as a result of interference between two waves traveling in opposite directions). The corresponding phenomenon in the atmosphere can be explained as follows: suppose that we have a stable stratified boundary layer, and it gets disturbed by sudden wind variations. Due to the disturbances, horizontal (and vertical later) motion results about the equilibrium layer (boundary layer) which travels along until it is reflected back from one of the end semi-enclosed basin. This interferes with the vertical disturbances and gives rise to standing waves, that is, the sloshing motion of the wind within the basin. These sloshing motions can be seen even as wind, pressure and temperature fluctuations within the basin [30].

# **CHAPTER 3**

## **EXPERIMENT**

In the first section of this chapter, the different sensors and the data logger employed during the experiment will be discussed. The details of the experiment setup and the time-line of operation of the instruments will be dealt with in the second section.

### **3.1 Instruments and Data Acquisition**

In this section, the operating principle and construction of the sensors, namely the quartz crystal barometers and a ultrasonic anemometer are discussed, along with the atmospheric parameters that these sensors measure. Following that, the setup and operation of the data logger is explained.

#### **3.1.1 Quartz Crystal Barometers**

The quartz crystal barometers (Intelligent Transmitters Series 6000) are manufactured by Paroscientific, Inc., Redmond, Washington. The operational features and the construction details of these sensors, explained in this thesis, are taken from the manufacturer's web site ([www.paroscientific.com](http://www.paroscientific.com)) and the sensor user's manual. These Paroscientific Intelligent Transmitters comprise of a Digiquartz pressure transducer and a digital interface board in a single package.

The Digiquartz pressure transducer is an inherently-digital and high precision instrument. It has a resolution of better than 0.0001%. The other improved features include low power consumption, high-reliability and long-term stability. These transducers employ a precision quartz crystal resonator (load-sensitive resonators) whose frequency of oscillation varies with the stress caused by the pressure fluctuations. The resonant frequency outputs of the resonator are detected using oscillator electronics similar to those employed in precision counters and clocks. A Double-Ended Tuning Fork system consisting of two identical beams driven piezoelectrically in 180° phase opposition is used. The resonant frequency of the resonator is a function of the applied load - increasing with tension and decreasing with compressive forces. The in-built temperature sensor consists of piezoelectrically-driven, torsionally oscillating tines whose resonant frequency is a function of temperature. Accuracy over a wide range of temperatures is achieved by thermally compensating the calculated pressure.

Bellows or Bourdon tubes are used in the pressure transducers as the pressure-to-load converters. Pressure acting on the effective area of the bellows generate a force and torque about the pivot and compressively stress the resonator. The change in applied pressure (fluctuation) proportionally changes the frequency of the quartz crystal oscillator. The pressure applied to the Bourdon tube generates an uncoiling force that applies tension to the quartz crystal to increase its resonant frequency. Acceleration compensation is provided, to reduce the effects of shock and vibration, to all the mechanisms using balance weights. In order to achieve the maximum resonator Q factor, these transducers are hermetically sealed and evacuated to eliminate air damping. Intelligent micro-processors are included with counter-timer circuitry to measure transducer (resonator) frequency outputs, to store the linearizing (start-stop and regression-line algorithms) and thermal compensation algorithm, calibration coefficients, and the command and control software to present the outputs in different

digital formats.

The digital interface board inside the Intelligent transmitter is used to receive or send commands and data requests through a two-way RS-232 or RS-485 serial interface. These dual RS-232 or RS-485 interface allows for the remote configuration and control of the parameters like resolution, sampling rate, choice of the units and integration time. Outputs are provided directly in engineering units with typical accuracy of 0.01% over a wide range of temperatures. The Intelligent transmitter series 6000 also has a high performance optional pressure port called the DigiPort. The DigiPort is used to reduce the effects of wind induced pressure fluctuations on the barometer output. The DigiPort has an environmentally rugged design that minimizes pressure errors under dynamic wind conditions. It provides accuracy of better than  $\pm 0.08$  hPa in strong winds, rain and freezing conditions and outmatches the open port sensors.

The latest firmware update with these Intelligent transmitter 6000 series gives the user the option of selecting the type of algorithm used to determine the frequency of the resonator: (1) the *start-stop* algorithm or (2) the *regression line* algorithm. It also gives the user the opportunity to increase the internal clock counter frequency by a factor of 4. The default internal counter clock frequency is 14.7 MHz. The use of the regression line algorithm or increased internal clock counter frequency results in improved resolution. In the following paragraph, the two algorithms for the frequency counters are explained.

The start-stop method of frequency counting uses reciprocal counting, which is based on measuring the time between two identical trigger points on the input signal. The number of input signal cycles  $N_s$  and the number of clock pulses from the built-in in-

ternal counter clock  $N_c$  are counted between the start and stop trigger events. There is an unavoidable dead time between each start and stop measurement for outputting the results, resetting the registers and preparing for the next measurement. The built-in processor then calculates the resonant frequency  $f_r$  of the transducer using

$$f_r = \frac{N_s}{N_c} f_c \quad (3.1)$$

where  $f_c$  represents the internal counter clock frequency used (default or quadrupled).  $N_s$  is always an exact integer since the counting is synchronized with the input signal and not with the clock pulses: which means, the measurement is totally unsynchronized with the clock pulses which could result in parts of clock pulse periods sometimes being counted and sometimes not counted. The resolution in the time measurement,  $N_c/f_c$ , for start-stop algorithm is therefore one clock pulse period ( $1/f_c$ ). A straightforward method of improving the resolution is to increase the clock frequency  $f_c$ . It can also be improved using the regression line algorithm of frequency counting instead of the start-stop algorithm. In the regression line algorithm of frequency counting, there is continuous counting of the input trigger events and the clock pulses without interruptions. At regular intervals called the pacing intervals, the fleeting contents of the respective registers are read in flight without interrupting the counter. The read values are stored in a fast memory. The readout instant is always synchronized with the input trigger so that the number of counted input cycles is always an integer. Similar to the reciprocal counter (start-stop), the uncertainty is in the reading out of the number of clock cycles. In this counter, after a certain measurement time has elapsed, there are many values of  $N_s$  and  $N_c$  between the start and stop events, not just the values at the start and stop trigger events. Thus, in the case of start-stop algorithm, the inclination of the plot of  $N_c/f_c$  versus

the input event counts is the average period. The resolution, that is the uncertainty of the line's inclination, depends only on the uncertainty of  $N_c/f_c$  at the start and stop points. In the case of counters employing a regression line algorithm, we have a number of points (instead of two points unlike start-stop), each having a certain resolution. Using the statistical method of *linear regression*, a linear line is fit to the set of points and in this way the uncertainty of the line's inclination and hence the measurement resolution is improved.

### 3.1.2 Ultrasonic Anemometers

The Ultrasonic anemometers (Model 81000) are manufactured by R. M. Young company, Traverse City, Michigan. These sensors measure wind speed, wind direction and temperature. Ultrasonic anemometers, as the name suggests, use ultrasonic acoustic waves to measure wind speed and direction. The model 81000 measures the three dimensional wind velocity and speed of sound based on the transit times of sound waves between three pairs of transducers (one for each dimension). Consider one pair of these ultrasonic transducers and let them be named  $U_1$  and  $U_2$ . Let  $v$  be the wind speed along the axis comprising the two transducers and assume that the direction is from  $U_1$  to  $U_2$ . An ultrasonic sound pulse is generated by  $U_1$  and the time  $t_{12}$  (in seconds) taken for the pulse to reach  $U_2$  is measured. Similarly, the time  $t_{21}$  taken for a ultrasonic sound pulse to reach  $U_1$  from  $U_2$  is measured. If  $d$  is the separation between the two transducers and  $c_{air}$  the speed of sound in air, the following equations result:

$$c_{air} + v = \frac{d}{t_{12}} \quad (3.2)$$

and

$$c_{air} - v = \frac{d}{t_{21}}. \quad (3.3)$$

The above equation pair can be solved for  $v$  and for  $c_{air}$ :

$$v = \frac{d}{2} \left[ \frac{1}{t_{12}} - \frac{1}{t_{21}} \right] \quad (3.4)$$

$$c_{air} = \frac{d}{2} \left[ \frac{1}{t_{12}} + \frac{1}{t_{21}} \right] \quad (3.5)$$

The magnitude of  $v$  is the wind speed ( $\text{ms}^{-1}$ ) and the sign of  $v$  determines the direction of wind. If  $v$  is positive, the direction of wind is as assumed (from  $U_1$  to  $U_2$  along the axis). In the case of  $v$  being negative, the direction of wind is from  $U_2$  to  $U_1$ . Having measured the wind speed and direction, the temperature  $T$  (in  $^{\circ}\text{C}$ ) can be obtained from the measured speed of sound  $c_{air}$  using the equation [17]

$$T = 273.15 \left[ \left( \frac{c_{air}}{331.3} \right)^2 - 1 \right] \quad (3.6)$$

Data output rates between 4 Hz and 32 Hz are possible with the model 81000 anemometers. Measured data are available as serial outputs using RS-232 or RS-485 cables. A variety of in-built serial output data formats are available including a custom format that can be easily set by the user. The strut opposite to the junction box on the anemometer is made to point in the North direction. The anemometer measures the wind velocities  $u$  (East-West),  $v$  (North-South) and  $w$  (vertical direction; bottom-top) and the temperature  $T$  (in  $^{\circ}\text{C}$ ). The model 81000 anemometer can

measure wind speeds of up to  $40 \text{ ms}^{-1}$  with a resolution of  $0.01 \text{ ms}^{-1}$  and temperatures between  $-50 \text{ }^{\circ}\text{C}$  to  $+50 \text{ }^{\circ}\text{C}$  with  $0.01 \text{ }^{\circ}\text{C}$  resolution.

### 3.1.3 Data Logger

A data logger of the type described in [4] was used during the experiment to collect data from different sensors. The data logger has eight serial ports and hence can handle up to eight sensors operating simultaneously. The data lines from these eight serial ports are multiplexed using a low power consumption USB adapter. The logger has a built-in hard drive of 160 GB capacity. This large data storage space of 160 GB enables continuous operation for several months. For example, ultrasonic anemometers of the type mentioned before operating at the maximum sampling frequency of 32 Hz connected to all the eight serial ports will make the hard drive overflow only after four months of continuous operation [4]. Data from each serial port is written to a separate file on the hard drive. Accurate time stamping is provided by a Global Positioning System antenna (GPS) connected to the data logger via a separate serial interface. The GPS antenna used is manufactured by Motorola (Model M12+). The local PC clock, which determines the time stamp of the data, drifts away with time and hence it is repeatedly checked and corrected with respect to a reference clock (GPS). This repeated resetting of the local PC clock with respect to the reference clock is done automatically by a function in NTP (Network Time Protocol) [19]. Thus, the NTP task continuously ensures that the local PC clock is synchronized with the reference clock (GPS). The accuracy with which the NTP task synchronizes the PC clock still depends on the operating system software latencies and the accuracy of the reference clock itself. Since GPS clocks are considered to be accurate within a few hundred microseconds [18], the accuracy of the synchronization depends largely on the operating system software latencies. The testing of the time

stamping provided by this system showed that the offset between the local PC clock and the reference GPS clock stayed within  $\pm 10 \mu\text{s}$  [4].

The data logger also provides for online access which helps monitor the data in real-time and control the system operation. This feature is provided by a 802.11 b/g 54 Mbit s<sup>-1</sup> network card and a wired 10/100 Mbit s<sup>-1</sup> network connection. The option of wireless access is very useful particularly during severe weather conditions or in difficult terrain. The data logger is powered either by AC grid power (110 V) or using DC marine batteries (12 V). Since the data logger will be usually installed outside, it needs to be protected from precipitation, dust, winds and extreme radiative fluxes. To ensure this, the data logger was mounted inside a weather-resistant enclosure (Campbell Scientific) as shown in figure 3.1. Additional details and information on the data logger's construction and operation can be found in [4].

## 3.2 Experiment Setup and Timeline

A six-month long experiment was conducted in a travel trailer located north of Amherst, Massachusetts from Dec 2007 to Jun 2008. This experiment was conducted with the aims of: (1) quantifying the performance of the barometers for different modes of operation and (2) studying meteorological and geophysical phenomena. Three quartz crystal barometers (Intelligent Transmitters Series 6000, manufactured by Paroscientific, Inc.) were placed side by side, a few centimeters apart near a window, on a dining table inside the travel trailer. The data were collected using custom made data-logging systems, of the type in [4], via a serial interface to communicate with the sensors. During test runs of the barometers and the data logger inside the Knowles Engineering Building of the University of Massachusetts Amherst, it had

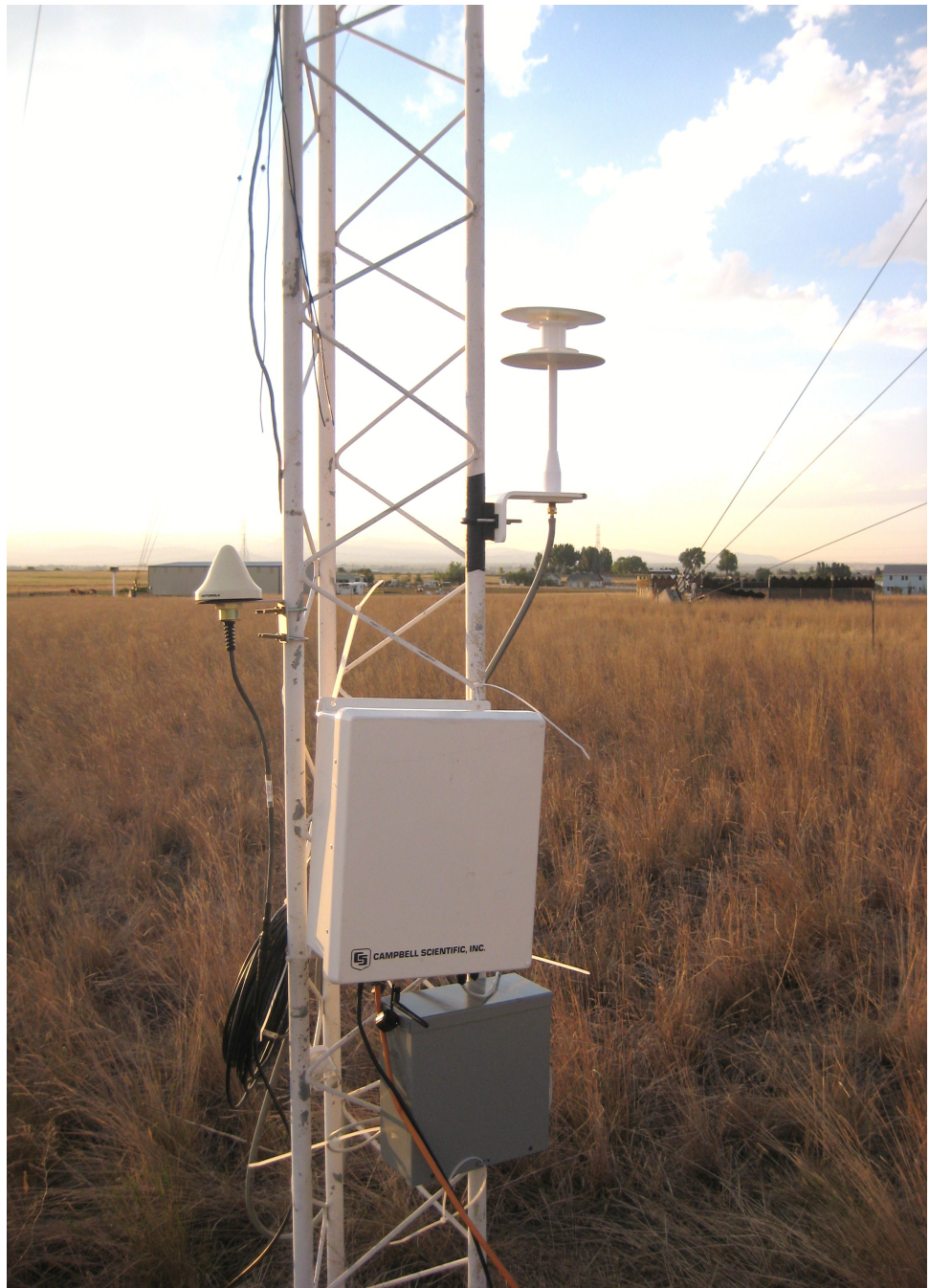


**Figure 3.1.** Data Logger in its protective enclosure by Campbell Scientific: The picture was taken during an experiment at the Boulder Atmospheric Observatory (BAO) near Erie, Colorado during Aug 2008. The DigiPort can be seen above the data logger on the right.

been observed that elevators, air-conditioning systems and the opening and closing of doors caused significant spikes in the pressure measured by the barometers. Hence, the trailer which was isolated from a building and from vehicular traffic seemed to be the a better test site. One ultrasonic anemometer (Model 81000, manufactured by R.M. Young Company) was mounted on a tripod mast just outside the trailer to monitor the weather conditions (temperature and wind measurements) during the course of the experiment. The anemometer's (referred to alternately as sonic) measurement volume center was at 2.0 m above ground level (AGL). The sonic measurements serve the purposes of: (1) measuring the wind speed and wind direction (to study their effects on pressure measured) and (2) measuring the temperature fluctuations. Accurate time stamping was provided by a Global Positioning System (GPS) antenna connected to the data logger(s), to correct the drift encountered in personal computer clocks. The GPS antenna was mounted on top of the trailer. Figures 3.3 and 3.4 show photographs of the experimental setup inside and outside the travel trailer respectively. The paragraphs to follow will give a detailed description of the timeline of the experiment and the operation of the sensors.

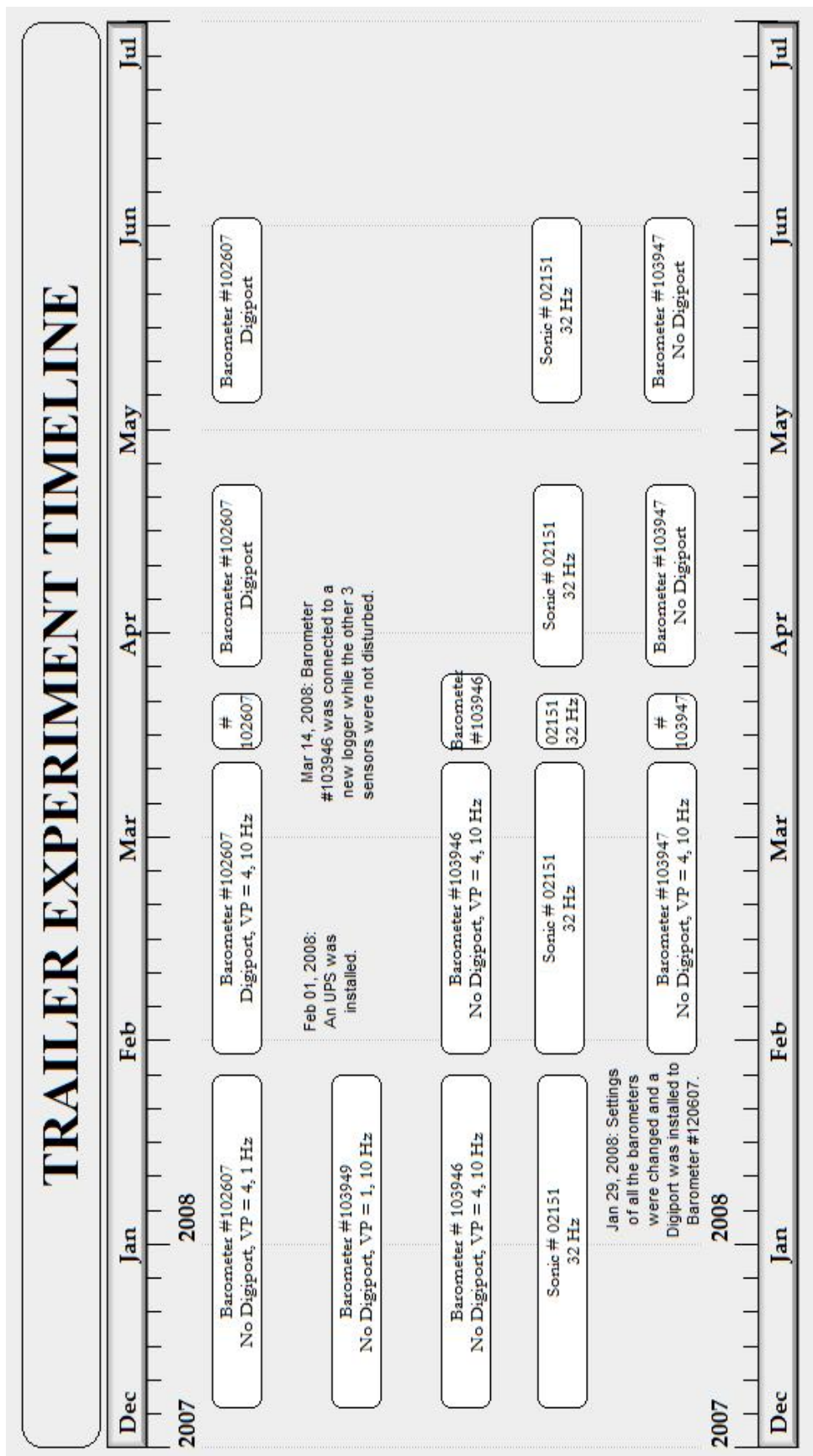


**Figure 3.2.** Graphical representation of the operational timeline of the sensors: It includes the operational timeline, with the respective settings, of each instrument used during the course of the experiment.

Figure 3.2 gives a graphical representation of the operational periods, with the respective settings, of each instrument employed during the experiment. Some important events have also been annotated in the graph. The exact dates during which the instruments were operational, along with their respective settings, have been presented in table 3.1.  $VP$  represents the clock counter frequency and  $XM$  represents the algorithm used. A value of 1 to  $XM$  means that the regression line algorithm was used while a value of 0 means that start-stop algorithm was used. The important events and the dates will be mentioned chronologically in the next paragraph.

The experiment was started on 07 Dec, 2007, with all the sensors connected to one data logger (logger #1). On 26 Jan, 2008, a power outage caused the data logger to shut down. On 29 Jan, 2008, the logger was restarted and the settings of the barometers were changed (Table 3.1). A DigiPort was connected to barometer #102607 on the same date. Due to a firmware issue, the clock counter frequency ( $VP$ ) of the barometer #103949 could not be quadrupled. Hence, that barometer was replaced with barometer #103947 with quadrupled clock frequency ( $VP=4$ ). An Uninterruptible Power Supply (UPS) was installed on 01 Feb, 2008, to prevent future power outages from interrupting the operation of the logger and the instruments. On 12 Mar, 2008, the data logger #1 stopped logging due to a software issue. On 14 Mar, 2008, a second data logger (referred henceforth as logger #2) was installed next to logger #1 to evaluate the accuracy of the GPS based time stamping between the two data loggers. The GPS antenna for the logger #2 was also mounted on the roof of the trailer. The barometer #103946 was disconnected from logger #1 and connected to logger #2. Data logging by logger #1 had stopped on 22 Mar, 2008, due to the same software issue as before. Data logging by logger #2 was not interrupted during that period. On 26 Mar, 2008, logger #2 and the barometer connected to it was taken back to the lab and logger #1 was restarted. There was continuous operation



**Figure 3.3.** Photograph of the barometers with data dogger inside the travel trailer: It shows the barometers (cube-like in blue color) with data logger (white colored box) on a table top.



**Figure 3.4.** Photograph of the travel trailer and the anemometer. The anemometer was mounted outside the trailer (left-side of the picture) and the picture was taken on 10 Dec 2007

**Table 3.1.** Timeline of operation of the sensors, along with their settings

Sensor Name	Start Date (mm/dd/yy)	End Date (mm/dd/yy)	$F_s$ (Hz)	VP	XM	Digiport (Y/N)
Sonic #02151	12/07/07	01/26/08	32	-	-	-
	01/29/08	03/12/08	32	-	-	-
	03/14/08	03/22/08	32	-	-	-
	03/26/08	04/22/08	32	-	-	-
	05/05/08	06/02/08	32	-	-	-
Barometer #103949	12/07/07	01/26/08	10	1	1	N
Barometer #103946	12/07/07	01/26/08	10	4	1	N
	01/29/08	03/12/08	10	4	1	N
	03/14/08	03/26/08	10	4	1	N
Barometer #103947	01/29/08	03/12/08	10	4	1	N
	03/14/08	03/22/08	10	4	1	N
	03/26/08	04/22/08	10	4	1	N
	05/05/08	06/02/08	10	4	1	N
Barometer #102607	12/07/07	01/26/08	1	1	1	N
	01/29/08	03/12/08	10	4	1	Y
	03/14/08	03/22/08	10	4	1	Y
	03/26/08	04/22/08	10	4	1	Y
	05/05/08	06/02/08	10	4	1	Y

of the logger between 26 Mar, 2008 and 22 Apr, 2008. The final continuous run was between 05 May, 2008 and 02 Jun, 2008, when the experiment was finished.

## CHAPTER 4

## DATA PROCESSING

### 4.1 Converting ASCII Data Files to MAT Files

The data logger stores the data from each of its sensors, over a day, as an ASCII data file (DAT extension) in the hard drive mounted within the data logger enclosure. At the beginning of each new day, according to the Coordinated Universal Time (UTC), a new file for that day is created and data is stored onto that file. The size of a file containing one complete day of barometer data depends primarily on the sampling frequency at which data is collected: greater the sampling frequency, larger the file size. The average size of an ASCII data file (DAT) that contains one complete day of barometer data with sampling frequency of 10 Hz is 60 MB. These data files contain data in ASCII format and have more than one type of delimiters. Few sample lines from one such data file for 06 Mar, 2008, are shown below.

```
2008 03 06 00 00 00.086239 *0004993.22734,50462
2008 03 06 00 00 00.086342
2008 03 06 00 00 00.190245 *0004993.22734,50455
2008 03 06 00 00 00.190329
2008 03 06 00 00 00.294245 *0004993.22768,50446
2008 03 06 00 00 00.294329
2008 03 06 00 00 00.402250 *0004993.22762,50439
2008 03 06 00 00 00.402360
2008 03 06 00 00 00.506253 *0004993.22741,50462
```

**Table 4.1.** Barometer data output format

YYYY	MM	DD	hh	mm	ss.ssxxxx	nnnn	ppp.ppppp	LLLLL
2008	03	06	00	00	00.086239	0004	993.22734	50462

The actual (valid) data is contained every alternate line, that is, every odd numbered line represents the actual data and the even numbered lines just represent the time stamp from the Global Positioning System (GPS) antenna. Each valid line of data is a combination of data from the barometer and the GPS antenna. It can be seen from the sample lines that there is more than one type of delimiter used to represent the data (space, comma and asterisk). Each valid line of data uses the following representation:

*YYYY MM DD hh mm ss.ssxxxx \*nnnnppp.ppppp,LLLLL*

where, *YYYY* - year, *MM* - month, *DD* - day, *hh* - hour, *mm* - minute, *ss.ssxxxx* - second (micro-second resolution), *nnnn* - sensor ID, *ppp.ppppp* - pressure (in hPa), *LLLLL* - latency. The variables *YYYY*, *MM*, *DD*, *hh*, *mm* and *ss.ssxxxx* are received from the GPS and the rest of the variables are received from the barometer. Using this representation, the data represented by the first line in the above sample is deciphered in the manner shown in table 4.1.

When the measured pressure is greater than 999.99999 hPa, an extra digit is assigned for the pressure string (*pppp.ppppp*). Sample data lines, at times when the measured pressure is greater than 999.99999 hPa, are shown below.

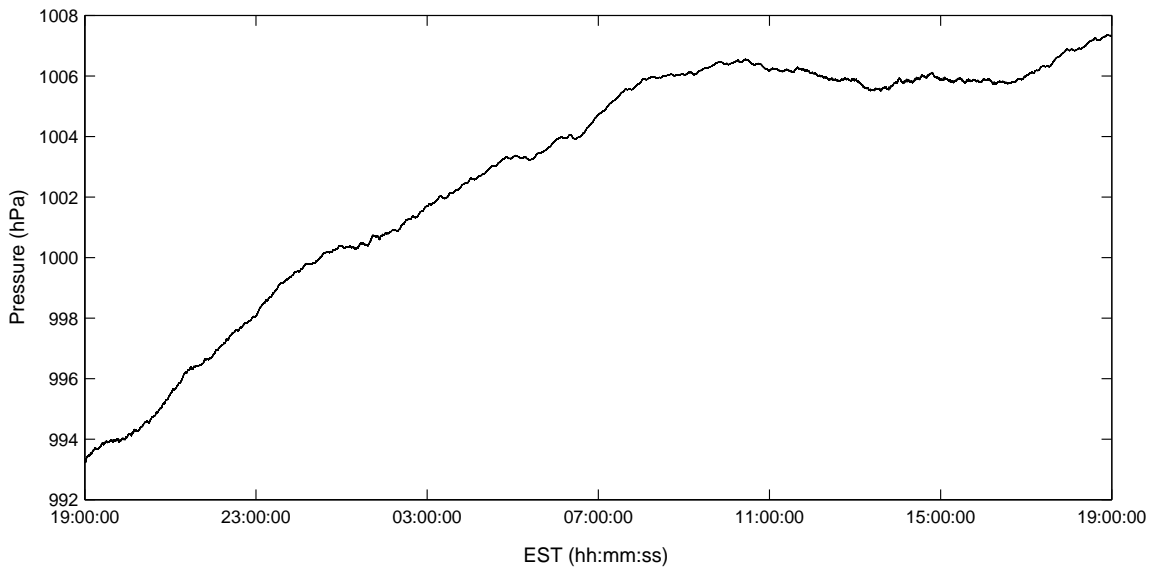


**Figure 4.1.** Pressure time series during a 24 h period: Time series of pressure between 1900 EST on 05 Mar, 2008 and 1900 EST on 06 Mar, 2008 measured by barometer #103947 with sampling frequency of 10 Hz.

2008 03 08 00 00 00.085793 \*00041001.48392,50409

2008 03 08 00 00 00.085891

2008 03 08 00 00 00.189697 \*00041001.48432,50407

2008 03 08 00 00 00.189785

2008 03 08 00 00 00.297714 \*00041001.48403,50428

2008 03 08 00 00 00.297825

2008 03 08 00 00 00.401795 \*00041001.48470,50423

In order to convert the DAT-file to a MAT-file, the data file format MATLAB uses for saving data to the hard disk, a program was written in MATLAB to convert the DAT-file into MAT-file format. A program was necessary (instead of directly importing the DAT-file onto MATLAB workspace) since more than one type of delimiter is used to represent the data in the DAT-file. The program loads the DAT-file and looks for the valid lines of data and stores the data to the corresponding arrays

namely  $YYYY$  - year,  $MM$  - month,  $DD$  - day,  $hh$  - hour,  $mm$  - minute,  $ss$  - second (micro second resolution),  $p$  - pressure (in hPa) and  $l$  - latency.

The arrays  $YYYY$ ,  $MM$ ,  $DD$ ,  $hh$ ,  $mm$  and  $ss$  are merged into one single array  $t$ , the serial date number, using the *datenum* command in MATLAB. A serial date number represents the whole and fractional number of days from a specific date and time, where *datenum*('Jan-1-0000 00:00:00') returns the number 1. Figure 4.1 shows the a 24 h long time series of pressure data from one of the barometers on 06 Mar, 2008. The arrays  $p$ ,  $t$  and  $l$  are stored in a MAT-file with the filename representing the barometer number and the day. The average size of the MAT-files containing one complete day of data recorded at 10 Hz is 6 MB.

## 4.2 Block Averaging to Obtain Equidistant Time Stamps

The barometer MAT-files contain non-equidistant time stamps in the time stamps array  $t$ , which is clear from the two sample data sections shown in the previous section. In order to obtain equidistant time stamps and hence, a constant sampling frequency, the data is subjected to block averaging. A constant sampling frequency is important for the computation of power spectrum and for discrete-time filtering. The application of block averaging to obtain equidistant time stamps will be explained in detail in this section.

Let  $T$  be the desired sampling time, that is, the time difference between consecutive data points. Data points in the interval (block) between the beginning of the day and  $T$  s later are chosen. Let  $p_{block}$  denote all the pressure data points in that

interval. The average of all the data points in  $p_{block}$  is computed, that is,

$$p_{avg} = \frac{1}{N} \sum_{i=1}^N p_{block}(i). \quad (4.1)$$

The time stamp assigned to the data point  $p_{avg}$ , is the mid time of the block under consideration, that is,

$$t_{avg} = t_{start} + \frac{t_{end} - t_{start}}{2} \quad (4.2)$$

where,  $t_{start}$  and  $t_{end}$  are the start and end time stamps of the interval (block) considered. Hence the data points in the interval between the beginning of the day and  $T$  s later are reduced to a single data point,  $p_{avg}$ , with  $t_{avg}$  being the corresponding time stamp.

The same procedure to compute the block averages and the corresponding time stamp is repeated for consecutive non-overlapping  $T$  s blocks of data. The block averaged pressure array,  $p_{avg}$ , along with the equidistant time stamps array,  $t_{avg}$ , over the entire day are stored in a separate MAT-file. In our case, the desired sampling time is taken as 0.5 s ( $T = 0.5$  s). The first four time stamps after block averaging, on 06 Mar, 2008, are shown in table 4.2 from which we can see that they are equidistant (0.5 s separation).

Figure 4.2 shows the averaged and non-averaged (actual) pressure data over a 10 s period on 06 Mar, 2008. It can be seen from the figure that the averaged pressure data has equidistant time stamps.

**Table 4.2.** Block averaged time stamps on 06 Mar, 2008

year	month	day	hour	minutes	seconds
2008	03	06	00	00	00.0003
2008	03	06	00	00	00.0008
2008	03	06	00	00	00.0013
2008	03	06	00	00	00.0018

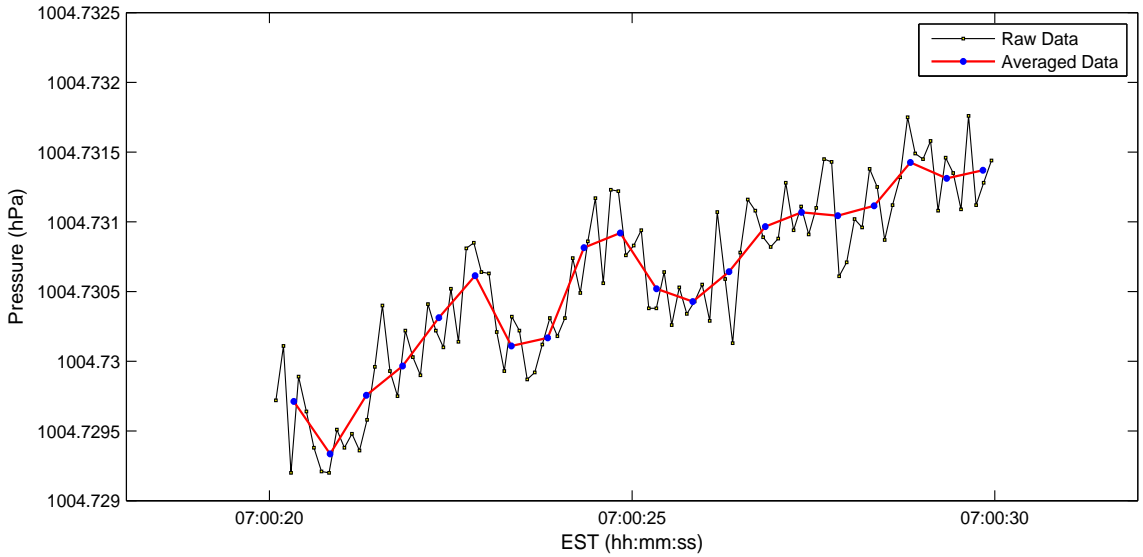


**Figure 4.2.** The averaged and non-averaged pressure data: A 10 s period of the averaged and non-averaged pressure data on 06 Mar 2008, shows that the 0.5 s averaged data (in red) clearly has equidistant time stamps.

### 4.3 Discrete Time Filtering

In this section, discrete time filtering of the block averaged pressure data for the filtering of microbaroms will be discussed. The design of discrete time FIR bandpass filter will be discussed in the following subsection and the application of the designed filter to the data will be discussed in the subsection after.

### 4.3.1 Design of Discrete-Time FIR Bandpass Filter

FIR filters have a finite duration impulse response and hence the name. The equations and some text used in this section are taken from section 10.2.2 of [25] and section 7.2 of [21]. The simplest method of FIR filter design is called the *windowing method*. In this method, an ideal desired frequency response is considered. Since ideal frequency responses are defined by piecewise-constant functions with discontinuities at the boundaries between the frequency bands, their impulse responses are noncausal and infinitely long. In order to make the impulse response finite in duration and causal, the ideal filter's impulse response is truncated using a window and delayed in time (samples). In this subsection, the design of a FIR bandpass filter by windowing is explained.

In the design of FIR filter by windowing, we begin with the desired frequency response,  $H_d(\omega)$ , and determine the corresponding impulse response,  $h_d[n]$ .  $H_d(\omega)$  and  $h_d[n]$  are related by the Fourier transform relation:

$$H_d(\omega) = \sum_{n=0}^{\infty} h_d[n]e^{-j\omega n} \quad (4.3)$$

where

$$h_d[n] = \frac{1}{2\pi} \int_{-\pi}^{\pi} H_d(\omega)e^{j\omega n}d\omega. \quad (4.4)$$

In the design of discrete time bandpass FIR filter, the desired frequency response,  $H_d(\omega)$ , is given by equation 4.5.

$$H_d(\omega) = \begin{cases} 0, & \omega \leq \omega_{c1} \\ 1, & \omega_{c1} \leq \omega \leq \omega_{c2} \\ 0, & \omega \geq \omega_{c2} \end{cases} \quad (4.5)$$

$h_d[n]$  is obtained using equation 4.4 and given by

$$h_d[n] = \frac{\omega_{c2}}{\pi} \text{sinc}(\omega_{c2}n) - \frac{\omega_{c1}}{\pi} \text{sinc}(\omega_{c1}n) \quad (4.6)$$

where, the function  $\text{sinc}(x)$  is defined as

$$\text{sinc}(x) = \begin{cases} 1, & x = 0 \\ \frac{\sin(\pi x)}{\pi x}, & x \neq 0 \end{cases} \quad (4.7)$$

and  $\omega$  is related to the continuous time frequency,  $F$ , and sampling frequency,  $F_s$ , by equation 4.8.

$$\omega_c = \frac{2\pi F_c}{F_s} \quad (4.8)$$

The desired impulse response obtained from equation 4.6 is infinite in duration and noncausal. In order to make it finite in duration, the straightforward method is to truncate the desired impulse response, say to length  $M$ . Truncation of the ideal desired impulse response to length  $M$  is equivalent to multiplying it with a *rectangular window*, defined by the equation 4.9 below .

$$w[n] = \begin{cases} 1, & 0 \leq n \leq M - 1 \\ 0, & \text{otherwise} \end{cases} \quad (4.9)$$

Thus, the impulse response of the causal FIR filter obtained by truncating the impulse response of the ideal filter is given by equation 4.10.

$$h[n] = h_d[n]w[n] \quad (4.10)$$

The effect of the rectangular window function on the desired frequency response  $H_d(\omega)$  can be visualized, considering the fact that the multiplication of  $h_d[n]$  and  $w[n]$  is equivalent to the convolution of  $H_d(\omega)$  with  $W(\omega)$ , where  $W(\omega)$  is the Fourier transform of the window function (equation 4.11).

$$W(\omega) = \sum_{n=0}^{M-1} w[n]e^{-j\omega n} \quad (4.11)$$

Thus the convolution of  $H_d(\omega)$  with  $W(\omega)$  yields the frequency response of the truncated (FIR) filter, that is,

$$H(\omega) = \frac{1}{2\pi} \int_{-\pi}^{\pi} H_d(\nu)W(\omega - \nu)d\nu. \quad (4.12)$$

The convolution of  $H_d(\omega)$  with  $W(\omega)$  has the effect equivalent to the smoothing  $H_d(\omega)$  with  $W(\omega)$ . As  $M$  is increased,  $W(\omega)$  becomes narrower and hence the smoothing provided is reduced. On the other hand,  $H(\omega)$ , the frequency response of the windowed filter, has relatively larger sidelobes due to the large sidelobes of  $W(\omega)$ .

These undesirable effects can be significantly reduced by the use of window functions that do not contain abrupt discontinuities in the time-domain and have relatively low sidelobes in the frequency-domain (page 666 of [25]). In the design to follow, a *Blackman window* is used since it has a relatively better sidelobe suppression among the different window functions (peak sidelobes of -57dB). The Blackman window function is given by the equation that follows.

$$w[n] = \begin{cases} 0.42 - 0.5 \cos\left(\frac{2\pi n}{M-1}\right) + 0.08 \cos\left(\frac{4\pi n}{M-1}\right), & 0 \leq n \leq M-1 \\ 0, & otherwise \end{cases} \quad (4.13)$$

In most cases, it is desirable to have a causal FIR filter with generalized linear phase response. It can be seen that the window defined by the above equation is symmetric about the point  $(M-1)/2$  shown mathematically in equation 4.14.

$$w[n] = \begin{cases} w[M-n], & 0 \leq n \leq M-1 \\ 0, & otherwise \end{cases} \quad (4.14)$$

If the desired impulse response  $h_d[n]$  is also symmetric about the point  $(M-1)/2$  (that is if  $h_d[n] = h_d[M-n]$ ), the windowed impulse response  $h[n]$  will also have symmetry about the point  $(M-1)/2$ . Hence, the windowed frequency response  $H(\omega)$  will have a generalized linear phase, that is,

$$H(\omega) = A_e(\omega)e^{-j\omega(M-1)/2} \quad (4.15)$$

where,  $A_e(\omega)$  is real and an even function of  $\omega$ . Hence, to make the desired impulse response symmetric about the point  $(M-1)/2$ , it is delayed by  $(M-1)/2$  sample points, that is,

$$\bar{h}_d[n] = h_d[n - (M - 1)/2], \quad 0 \leq n \leq M - 1. \quad (4.16)$$

Now,  $\bar{h}_d[n]$  is windowed with the window function  $w[n]$  using equation 4.10 and let the windowed impulse response obtained be  $\bar{h}[n]$ . This impulse response is finite in duration, causal and symmetric about the point  $(M-1)/2$ . Furthermore, the DC bias introduced in the filtered output (during the windowing operation) is removed so that the filtered output is a zero-mean sequence. The new impulse response is given by the following equation.

$$\tilde{h}[n] = \bar{h}[n] - \frac{1}{M} \sum_{k=0}^{M-1} \bar{h}[k], \quad 0 \leq n \leq M - 1 \quad (4.17)$$

Thus,  $\tilde{h}[n]$  is the impulse response of the FIR bandpass filter designed by windowing such that the DC bias, that will be added to the filtered output, is compensated for in the impulse response itself.

#### 4.3.2 Filtering using Discrete-Time FIR Filter

In this section, the parameters of the discrete-time FIR bandpass filter will be determined and the resulting filter will be used for detecting microbaroms in the block averaged pressure data  $p_{avg}$ . In order to design a filter to detect microbaroms which have periods of about 5 s (sometimes goes up to about 8 s [23]), the cutoff

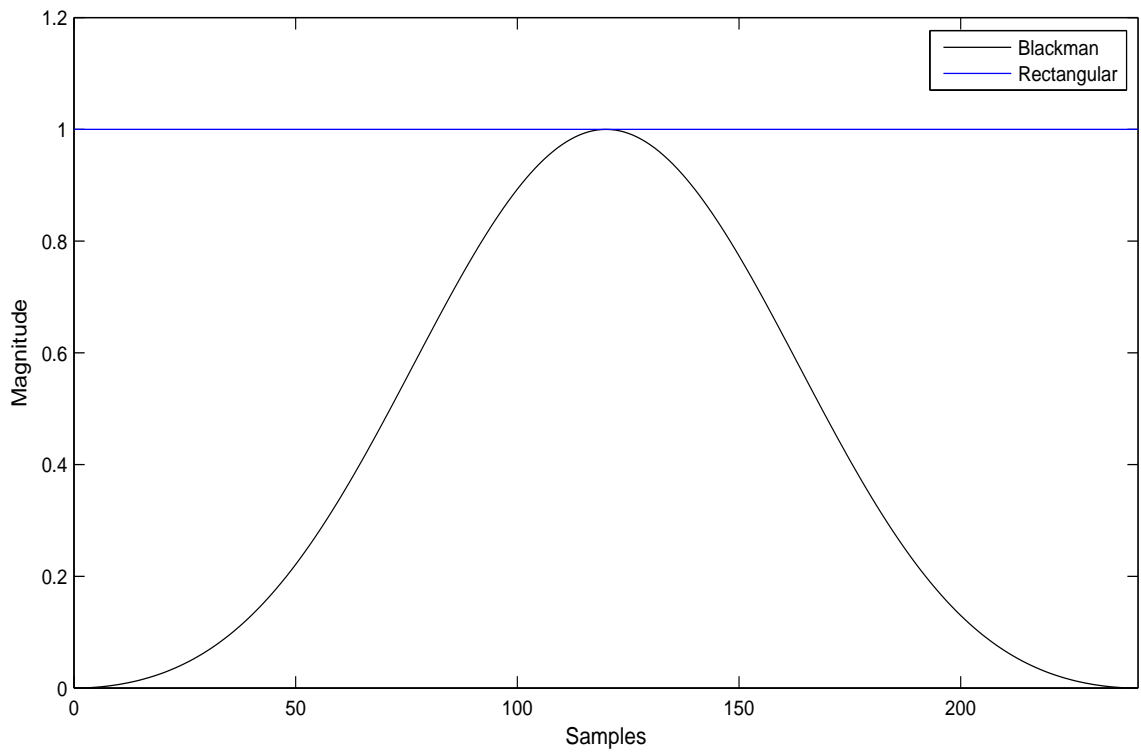
**Table 4.3.** Parameters of the FIR bandpass filter for the microbaroms

$F_{c1}$	$F_{c2}$	$F_s$	$\omega_{c1}$	$\omega_{c2}$	$M$	Window type
0.1 Hz	0.5 Hz	2 Hz	$0.1\pi$	$0.5\pi$	241	Blackman

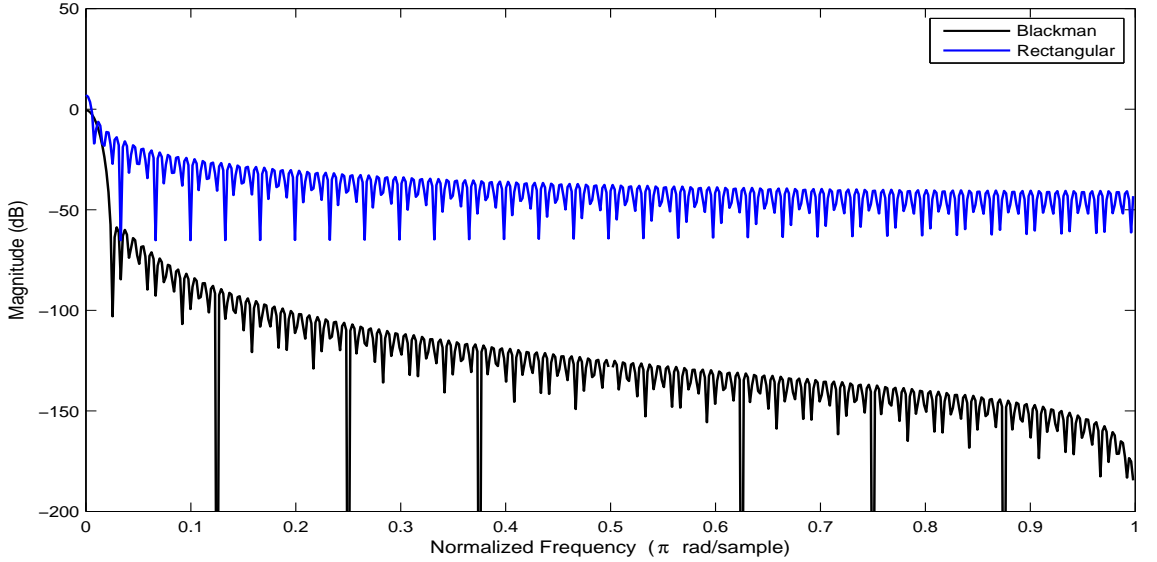
frequencies  $F_{c1}$  and  $F_{c2}$  are chosen to be 0.1 Hz and 0.5 Hz respectively. Since the sampling frequency  $F_s$  of the block averaged pressure data,  $p_{avg}$ , is 2 Hz, the values of  $\omega_{c1}$  and  $\omega_{c2}$  (using equation 4.8) are  $0.1\pi$  and  $0.5\pi$  respectively. The length,  $M$ , of the window function and hence that of the FIR filter is determined considering the fact that the window needs to include a few periods of the microbaroms, that is it must have a duration of at least 60 s. Hence, a window duration of 120.5 s was chosen which corresponds to a value of 241 for  $M$ . Figure 4.3 illustrates the shape and time domain characteristics of the Blackman and rectangular windows. It can be seen that both the windows are symmetric about the point  $(M-1)/2$ . Table 4.3 contains the parameters of the FIR bandpass filter designed to detect microbaroms.

Figure 4.4 illustrates the magnitude response of the rectangular and Blackman windows. It is clear that the rectangular window has a narrow main lobe but has a poor side lobe level relative to the Blackman window. Figure 4.5 shows the frequency response of the designed bandpass filter. It can be seen that the side lobe level is less than -50 dB which is about the expected value when a Blackman window is used.

The filtering operation is nothing but the convolution of the input signal with the impulse response of the filter. If  $p_{avg}$  is the mean removed ( $p_{avg} - \text{mean}(p_{avg})$ ) input to the discrete-time FIR bandpass filter with impulse response  $\tilde{h}[n]$ , then the filtered output  $p_{avg}^{fil}$  is given by the equation that follows.



**Figure 4.3.** Rectangular and Blackman windows in the time domain. The window length  $M$  is selected to be 241. It is clear that both the windows are symmetric about the mid point of the window length.



**Figure 4.4.** Magnitude response of the rectangular and Blackman windows. It is apparent that the rectangular window has a narrower main lobe width and the Blackman window has a better side lobe level. The window width is 241 samples.

$$p_{avg}^{fil}[n] = p_{avg}[n] * \tilde{h}[n] \quad (4.18)$$

where, the symbol  $*$  represents *convolution sum*, that is, the output of the filter is the convolution of the input,  $p_{avg}$ , with  $\tilde{h}[n]$ , the impulse response of the filter. The resulting output has a phase delay of  $(M-1)/2$  samples which is linear. Hence, the output samples are advanced by  $(M-1)/2$  sample points to neutralize the effect of the linear phase introduced by the filter system, that is, if  $t_{avg}$  is the time stamps array corresponding to the input array,  $p_{avg}$ , then  $t_{avg}[n]$  will be the time stamp of  $p_{avg}^{fil}[n+(M-1)/2]$ . Also, the first and the last  $(M-1)/2$  points of the filtered output are removed in order to disregard the transient effects of the filtering operation.

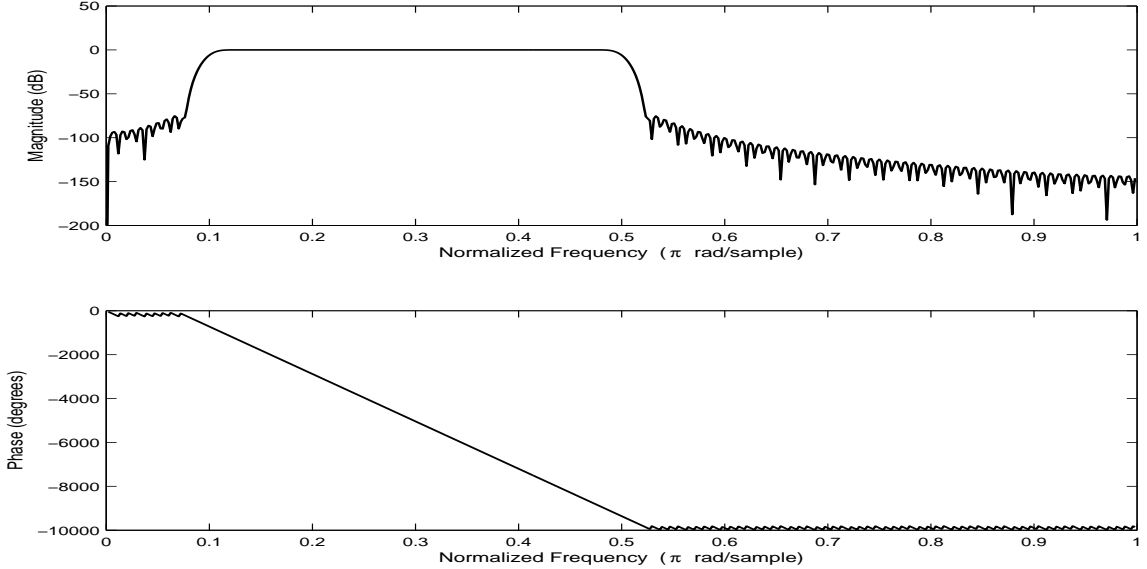


**Figure 4.5.** Frequency response of the bandpass filter for the microbaroms: the side lobe level (top figure) is less than -50 dB which is the expected value when Blackman window is used. Also, the filter has a linear phase response (bottom figure).

#### 4.4 Power Density Spectrum and Coherence Function

Meteorological phenomena such as the fluctuations in pressure and air temperature are characterized as random processes. To characterize such random processes, the concentration is on the average characteristics of the random signal. In the time domain, the autocorrelation function of a random process is the best statistical average that characterizes the random signal. In the frequency domain, the Fourier transform of the autocorrelation function, namely the power density spectrum is used to characterize random signals. The equations and some text used in this section are adopted from chapter 14 of [25] and chapter 10.6 of [21]. In the following sections, the estimation of the power spectrum of random signals and the *Welch's method* of power spectrum estimation will be explained. Later in the section, the estimation of the coherence function between two random signals is explained.

#### 4.4.1 Estimation of the Power Spectrum of Random Signals

The classes of signals characterized as stationary random processes do not have finite energy and hence they do not possess a *Fourier transform*. Such signals have finite average power and are characterized by the power density spectrum. Let  $x_a(t)$  be a continuous time random signal (a single realization of the random process) and  $x[n]$ ,  $0 \leq n \leq N-1$ , be the finite-duration sequence obtained by sampling  $x_a(t)$  at a rate  $F_s$  Hz. An estimate of the power density spectrum  $P_{xx}(\omega)$  of  $x[n]$  is given by the following equation.

$$P_{xx}(\omega) = \frac{1}{N} \left| \sum_{n=0}^{N-1} x[n] e^{-j\omega n} \right|^2 = \frac{1}{N} |X(\omega)|^2 \quad (4.19)$$

where,  $X(\omega)$  is the Fourier transform of  $x[n]$ . This form of the power density spectrum estimate is called the *periodogram* which was introduced by Schuster in 1898 [26] to detect and measure hidden periodicities in data. This power density spectrum estimate  $P_{xx}(\omega)$  of the stationary discrete-time random signal  $x[n]$  is proportional to the power density spectrum estimate  $S_{xx}(\Omega)$  of the continuous time random signal  $x_a(t)$ , that is,

$$P_{xx}(\omega) = \frac{1}{T} S_{xx}(\Omega). \quad (4.20)$$

where,  $T$  is the sampling period at which  $x_a(t)$  is sampled. As can be seen from page 970 of [25], the variance of the power density spectrum estimate does not decay to zero as  $N \rightarrow \infty$ . Hence, it can be concluded that the periodogram is not a consistent estimate of the true power density spectrum, that is, it does not converge to the true power density spectrum. Thus, the classical nonparametric power spectrum estimation methods formulated by Bartlett (1948) [2], Blackman and Tukey (1958) [7] and Welch (1967) [29] which makes no assumption about the data sequence are

used for the estimation of power density spectrum.

#### 4.4.2 Welch's Method: Averaging Modified Periodogram

This method [29] makes no assumption about how the data were generated and hence is called a nonparametric method of power spectrum estimation. The nonparametric methods decrease the frequency resolution in order to make the variance in the spectral estimate as low as possible. In Welch's method of averaging modified periodogram, the first step is to divide the  $N$ -point data sequence into  $K$  overlapping segments with each segment having a length  $L$ .  $R$  represents the number of non-overlapping points between consecutive segments. The data segments are thus represented by,

$$x_i[n] = x[n + iR], \quad 0 \leq n \leq L - 1, \quad 0 \leq i \leq K - 1 \quad (4.21)$$

where,  $iR$  is the starting point of the  $i$ th segment. If  $R$  equals  $L$ , the segments do not overlap and if  $R$  equals  $0.5L$ , there is 50% overlap between successive segments. Once the  $N$ -point data sequence is subdivided into  $K$  overlapping segments, the next step in the Welch's method is to window the data segments with a window  $w[n]$ . When the window  $w[n]$  is not a rectangular window, the spectral estimate obtained is called the modified periodogram, given by,

$$\tilde{P}_{xx}^{(i)}(\omega) = \frac{1}{LU} \left| \sum_{n=0}^{L-1} x_i[n]w[n]e^{-j\omega n} \right|^2, \quad 0 \leq i \leq K - 1 \quad (4.22)$$

where,  $U$  is the normalization factor for the power in the window function used and is given by equation 4.23.

$$U = \frac{1}{L} \sum_{n=0}^{L-1} (w[n])^2 \quad (4.23)$$

For a rectangular window,  $U$  is chosen to be 1, while for other window functions (for which  $w[n]$  is normalized to a maximum value of 1),  $U$  is in the interval  $0 < U < 1$ . Thus, periodogram samples can be obtained at discrete frequencies by replacing the discrete-time Fourier transform of  $w[n]x_i[n]$  in equation 4.22 by the discrete Fourier transform (DFT). Thus, the equation 4.22 changes to

$$\tilde{P}_{xx}^{(i)}(\omega_k) = \frac{1}{LU} |V_i[k]|^2 \quad (4.24)$$

where,  $V_i[k]$  is the  $M$ -point DFT of  $w[n]x_i[n]$ . Thus, samples of the periodogram at DFT frequencies  $\omega_k = 2\pi k/M$ , for  $k = 0, 1, \dots, M-1$ , are obtained using the above equation 4.24. The value of  $M$  has to be greater than or equal to the length of each segment,  $L$ , and appropriate zero-padding needs to be applied to  $w[n]x_i[n]$  in the former case.

If the random signal has a nonzero mean, the estimated power density spectrum will have an impulse at zero frequency. If the mean is relatively large, it will dominate the spectrum estimate and hence obscure the low-amplitude components and the low-frequency components (near zero frequency). Hence, in practice, the mean is estimated using

$$\hat{m}_x^{(i)} = \frac{1}{L} \sum_{n=0}^{L-1} x_i[n] \quad (4.25)$$

and is subtracted from the random signal before computing the power density spectrum estimate. This leads to a better estimate at frequencies close to the zero-frequency although the mean is only an approximate estimate of the zero-frequency component. Thus,  $x_i[n]$  used in the preceding equations represents the  $i$ th segment of  $x[n]$ , with the sample mean  $\hat{m}_x^{(i)}$  subtracted from each of its samples. The last step in Welch's method of power spectrum estimation is the averaging of the modified periodograms over the  $K$  segments, that is

$$P_{xx}^W(\omega_k) = \frac{1}{K} \sum_{i=0}^{K-1} \tilde{P}_{xx}^{(i)}(\omega_k), \quad k = 0, 1, \dots, M-1 \quad (4.26)$$

where,  $P_{xx}^W(\omega_k)$  is the averaged modified periodogram or Welch's power spectrum estimate at frequency  $\omega_k$ . The percentage of overlap between successive segments can be varied in an attempt to reduce the variance of the estimate to as low a value as possible.

The computation of the power density spectrum estimate of the averaged pressure data,  $p_{avg}[n]$ , is done using the Welch method. The averaging is done over, say a 1 h period, that is,  $p_{avg}[n]$  is cut down to only 1 h of data. As mentioned in section 4.3.2, the window duration has to be at least 60 s. Hence, a Blackman window of 60 s duration and 50% overlap between successive segments (30 s overlap) is used, that is, a value of  $L = 121$  and  $R = 31$ . Now,  $p_{avg}[n]$  is subdivided into segments,  $p_i[n]$ , of length  $L$  with  $R$  point overlap between successive segments. Since we are interested in the microbarom frequency band of 0.1 Hz to 0.5 Hz, it is very important that the

mean is subtracted from each of the segments (as explained earlier in this section), that is,

$$\tilde{p}_i[n] = p_i[n] - \frac{1}{L} \sum_{k=0}^{L-1} p_i[k], \quad 0 \leq i \leq K-1 \quad (4.27)$$

where,  $\tilde{p}_i[n]$  is the zero mean  $i$ th segment of  $p_{avg}[n]$ . The next step is to window each  $\tilde{p}_i[n]$  with  $w[n]$  and compute the modified periodogram,  $\tilde{P}_{pp}^{(i)}(\omega_k)$ , of all the  $K$  segments given by the equation 4.28.

$$\tilde{P}_{pp}^{(i)}(\omega_k) = \frac{1}{LU} \left| \sum_{n=0}^{L-1} \tilde{p}_i[n] w[n] e^{-j\omega_k n} \right|^2, \quad 0 \leq i \leq K-1, k = 0, 1, \dots, M-1 \quad (4.28)$$

The final step is the averaging of the modified periodograms over the  $K$  segments, thus obtaining the averaged modified periodogram,  $P_{pp}^W(\omega_k)$ . This is the Welch power spectrum estimate (at frequency  $\omega_k$ ) of pressure fluctuations over the selected time duration of the data, 1 h in our example.

$$P_{pp}^W(\omega_k) = \frac{1}{K} \sum_{i=0}^{K-1} \tilde{P}_{pp}^{(i)}(\omega_k), \quad k = 0, 1, \dots, M-1 \quad (4.29)$$

Thus, the power density spectrum estimate  $S_{pp}^W(F_k)$ , at frequency  $F_k$ , of the corresponding continuous-time pressure signal  $p_{avg}(t)$ , using equation 4.20, is given by,

$$S_{pp}^W(F_k) = \frac{1}{F_s} P_{pp}^W(\omega_k), \quad k = 0, 1, \dots, M-1 \quad (4.30)$$

where,  $F_s$  is the sampling rate at which  $p_{avg}(t)$  is sampled. The corresponding continuous time frequencies,  $F_k$ , of the frequency vector  $F$  are obtained from the  $M$ -point ( $= L$ , the window length in our case) DFT frequencies  $\omega_k$  using equation 4.31.

$$F[k] = F_k = \frac{\omega_k F_s}{2\pi} = \frac{\omega_k}{2\pi T} = \frac{k}{MT}, \quad 0 \leq k \leq M - 1 \quad (4.31)$$

where,  $T$  is the sampling period of the pressure data and  $S_{pp}^W(F)$  has the unit of  $\text{Pa}^2\text{Hz}^{-1}$ . Thus, the two-sided power density spectrum,  $S_{pp}^W(F)$ , of the pressure data computed using Welch's method of averaging modified periodogram is obtained. To obtain a one-sided power density spectrum,  $S_{pp}^W(F)$  is scaled by a factor of 2, which will be used in the computation of the amplitude and frequency of microbaroms. Hence, throughout the rest of my thesis, unless explicitly stated, power density spectrum refers to the one-sided spectrum.

In a similar way, the Welch's method of averaging modified periodogram can be used to compute the cross-spectral density, which is the DFT of cross-correlation, between two  $N$ -point sequences  $x[n]$  and  $y[n]$ . Again, the two sequences are divided in to  $K$  overlapping segments. The cross-periodogram samples for each segment can be obtained at discrete frequencies (after windowing both the sequences  $x[n]$  and  $y[n]$ ) by modifying equation 4.24 slightly, given by,

$$\tilde{P}_{xy}^{(i)}(\omega_k) = \frac{1}{LU} V_i[k] \overline{Z_i[k]} \quad (4.32)$$

where,  $V_i[k]$  and  $Z_i[k]$  are the  $M$ -point DFTs of  $w[n]x_i[n]$  and  $w[n]y_i[n]$  respectively.  $\overline{Z_i[k]}$  represents the complex conjugate of  $Z_i[k]$ . Thus, samples of the periodogram at DFT frequencies  $\omega_k = 2\pi k/M$ , for  $k = 0, 1, \dots, M-1$ , are obtained using the

above equation 4.24. Hence, averaging  $\tilde{P}_{xy}^{(i)}(\omega_k)$  over the  $K$  segments gives the cross-spectrum estimate,  $P_{xy}^W(\omega_k)$ , at frequency  $\omega_k$ . Finally the one-sided cross-spectral density  $S_{xy}^W(F)$  can be obtained in a similar fashion as the one-sided power density spectrum.

The one-sided cross-spectral density and the individual power spectral density can be used to determine the *coherence function* (chapter 8.8.4 of [27]),  $\Gamma_{xy}(F)$ , given by equation 4.33.

$$\Gamma_{xy}(F) = \frac{S_{xy}^W(F)}{\sqrt{S_{xx}^W(F)S_{yy}^W(F)}} \quad (4.33)$$

The coherence function,  $\Gamma_{xy}(F)$ , is a measure of the extent to which the signals  $x$  and  $y$  are correlated at each frequency.

## 4.5 Computation of Microbarom Amplitude and Frequency

A typical power density spectrum of pressure fluctuations (when microbaroms are observed) contains a distinct peak: the existence of such a distinct peak in the microbarom frequency range of 0.15 Hz to 0.3 Hz confirms the occurrence of microbaroms. The frequency corresponding to this peak is considered the peak microbarom frequency. Since the energy of the microbarom is spread over the frequency band of 0.15 Hz and 0.3 Hz, the centroid frequency in the microbarom band is a better estimate of the microbarom frequency. When such a peak appears in the power density spectrum, confirming the existence of microbaroms, the power in the microbarom frequency band is computed and hence the amplitude of the microbarom. In this section, the methods of computing the microbarom amplitude and frequency are ex-

plained.

In the adaptive frequency band method, the averaged modified periodogram,  $S_{pp}^W(F)$ , is checked for the presence of a distinct peak in the microbarom frequency range of 0.15 Hz to 0.3 Hz. Once a peak is detected, the lower cutoff frequency of the microbarom band is fixed as the frequency (less than the peak frequency) at which the power spectral density attains a minimum. This is important because the power in the gravity wave band, sometimes, might contribute towards the amplitude of the microbaroms and hence, leading to its over-estimation. The upper cutoff frequency is fixed at 0.3 Hz. Then the power in the adaptive frequency band and the centroid frequency are computed and finally the amplitude of the microbaroms. In the case of non-occurrence of a microbarom peak, the microbarom centroid frequency and the amplitude are considered *NaN*, that is, *Not a Number*.

Another straightforward method (constant frequency band method) is to have the microbarom amplitude and centroid frequency computed over a constant frequency band of 0.1 and 0.3 Hz. The centroid frequency of the microbaroms,  $F_{mb}$ , is computed using the equation below.

$$F_{mb} = \frac{\sum_{k=F_l}^{F_u} S_{pp}^W(F_k) F_k}{\sum_{k=F_l}^{F_u} S_{pp}^W(F_k)} \quad (4.34)$$

$F_u$  and  $F_l$  represents the upper and lower cutoff frequencies of the microbarom band for the two methods used. The amplitude of the microbarom, if any, is computed by first computing the power,  $P_{mb}$ , in the microbarom frequency band using the equation below.

$$P_{mb} = \sum_{k=F_l}^{F_u} S_{pp}^W(F_k) \Delta F \quad (4.35)$$

$\Delta F$  is the spacing between two adjacent frequency points in the power spectral density. Having computed the power in the microbarom frequency band, the next step is to obtain the RMS amplitude of the microbarom,  $A_{mb}$ , using the relation below.

$$A_{mb} = \sqrt{2P_{mb}} \quad (4.36)$$

A time stamp, corresponding to the mid-time of the 1 h interval for which the periodogram is computed, is assigned to both  $A_{mb}$  and  $F_{mb}$ . Thus, time series of the microbarom centroid frequency and amplitude are obtained by repeating the same procedure explained above for successive 1 h averaged modified periodograms.

## 4.6 Spectrogram

Spectrogram is an image that demonstrates the variation of power density spectrum of a signal with time. The most common format is a plot with two geometric dimensions: the horizontal axis representing the *time* and the vertical axis representing the *frequency*. A third dimension that shows the intensity (amplitude) at a particular frequency at a particular time is represented by the *color* of that point in the image. It is also common to use varying intensities of the same color (like grayscale) instead of different colors. In some applications, it is common to represent the amplitude as the height of a 3D surface instead of varying intensity or color. Both the frequency axis and the intensity (amplitude) can be expressed in logarithmic and

linear scales. Spectrograms are generated from discrete sampled data by first computing the magnitude of the power density spectrum during a particular time interval using the Fourier transform. Power density spectrum for consecutive time intervals are then plotted as an image to form the spectrogram. In this section, the process of obtaining the spectrograms of the pressure fluctuations in the microbarom frequency band is explained.

The 1 h averaged modified periodograms computed in section 4.4.2 will be used in obtaining the spectrogram of the pressure fluctuations in the microbarom frequency band. Each 1 h modified averaged periodogram is assigned a time stamp corresponding to the mid-time of the 1 h interval. Thus, a matrix,  $S_{pp}^W(F,t)$ , containing the values of  $S_{pp}^W(F)$  as a function of time  $t$  is produced. Also the corresponding frequency array,  $F$ , of the periodogram, and the time stamp array,  $t$ , are formed. The final step is to plot the matrix  $S_{pp}^W(F,t)$  as an image with the horizontal and vertical axes values determined by the arrays  $t$  and  $F$  respectively. The values of  $S_{pp}^W(F,t)$  can be normalized to a constant reference value and these values are represented by different colors. The spectrograms serve as a useful tool for analyzing the variation of spectral characteristics of signals with time.

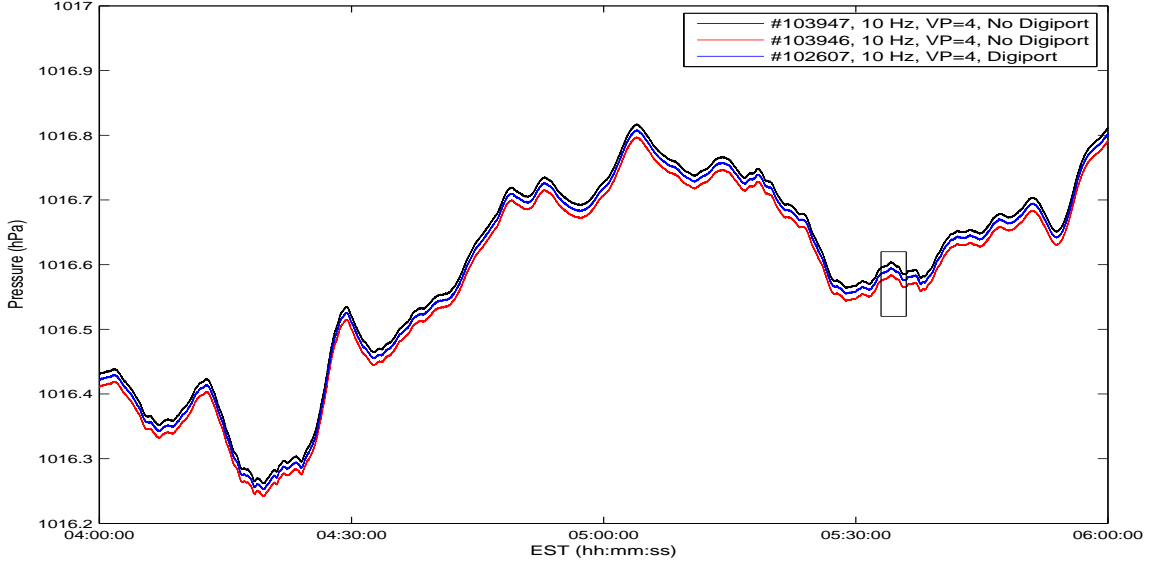
## CHAPTER 5

### RESULTS AND INTERPRETATION

In this chapter, the results obtained from the analysis of the data are presented and interpreted. In the first section, the first observations of ocean generated atmospheric infrasound ("microbaroms") using a single absolute barometer are presented. In the second section, the temporal variations of the frequency and amplitude of the microbaroms are analyzed and interpreted. The third and last section of this chapter addresses the overall performance of the barometers and the effectiveness of the DigiPort. Throughout this chapter, all times will be specified in Eastern Standard Time (EST). EST is preferred because the objective is to use a standard time based only on geographical location and solar time. Since daylight saving time is an artificially set time only during the summer months, EST will be used. EST is preferred over UTC because it gives a feel of the natural phenomena that we observe with respect to the local time.

#### 5.1 First Observations of Microbaroms using Single Absolute Barometers

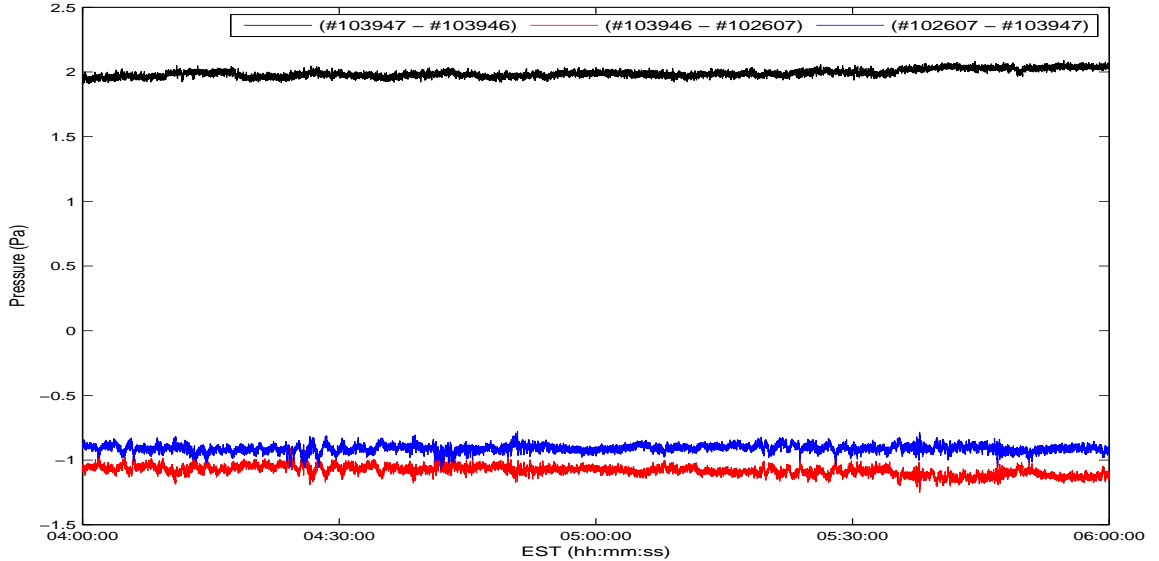
As described in chapter 2, microbaroms are generated by standing or nearly standing ocean surface waves, that is, superpositions of ocean surface waves, with nearly the same frequency and amplitude propagating in nearly opposite directions. Microbaroms have a typical frequency of 0.2 Hz, twice the frequency of the surface waves that generate them. In this section the first observations of microbaroms using a



**Figure 5.1.** Raw pressure time series over a 2-hr time interval: measured with three collocated barometers on March 18, 2008 between 0400 and 0600 EST.

single absolute barometer are reported.

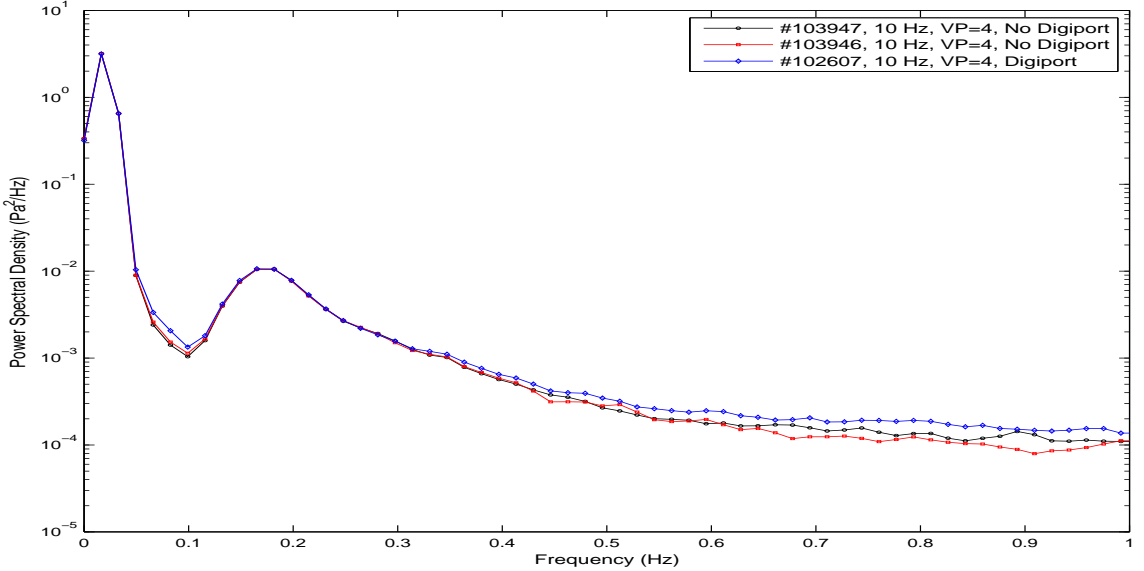
Figure 5.1 shows the time series of pressure measured by the three barometers between 0400 and 0600 EST on 18 Mar, 2008. The signal in blue is measured by the barometer with the DigiPort while the other two are measured by the barometers without the DigiPort. All the three barometers had their internal clock counter frequency quadrupled. In order to get an estimate of the relative accuracy between the sensors for short temporal-scales, the time series of the difference between each pair of the signals (in Figure 5.1) are shown in figure 5.2. The difference is almost constant with time between all the three pairs. The mean values of the black, red and blue curves are 1.990 Pa, -1.0803 Pa and -0.9097 Pa with standard deviations of 0.0289 Pa, 0.0371 Pa and 0.0289 Pa respectively. Fluctuations with periods up to about 3 minutes can be seen in the blue and red curves while only high frequency fluctuations can be observed in the black curve. This observation is consistent with



**Figure 5.2.** Time series of the difference between the three signals of figure 5.1: The mean values are 1.990 Pa, -1.0803 Pa and -0.9097 Pa with standard deviations of 0.0289 Pa, 0.0371 Pa and 0.0289 Pa respectively. When the barometer with DigiPort is involved, trends on the order of 1-3 min can be observed.

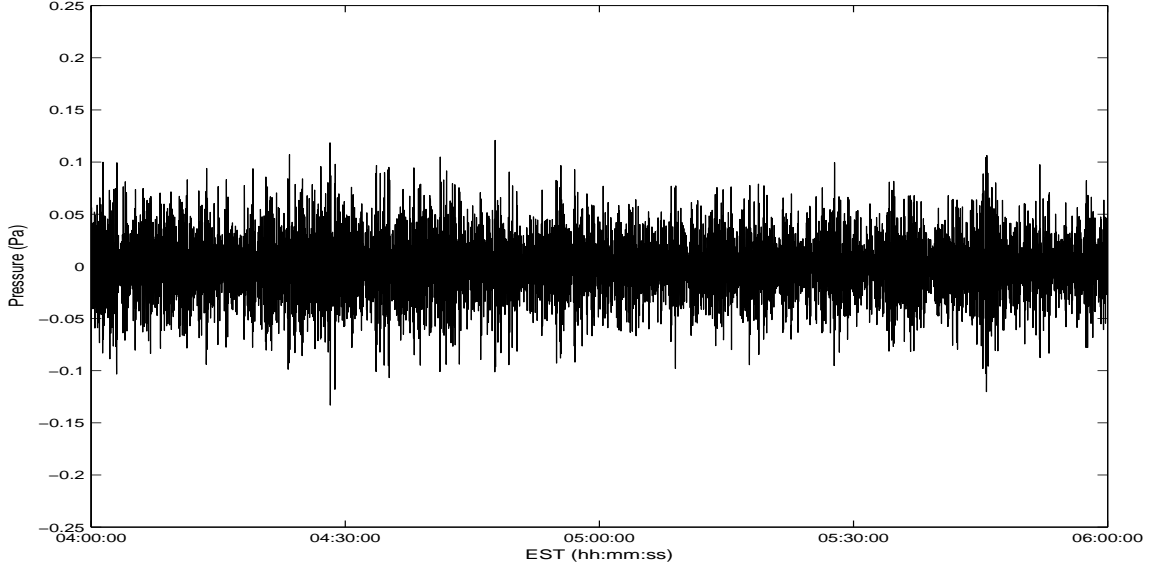
the fact that the two barometers without the DigiPort measure the pressure inside the travel trailer while the barometer with the DigiPort measures the pressure outside the trailer. The relatively low frequency fluctuations observed in the red and blue curves of figure 5.2 is related to the wind speed outside the trailer, which will be shown later in this chapter. It can be concluded from figures 5.1 and 5.2 that the relative accuracy between these barometers is of the order of a few pascals (few tenths of a microbar).

Figure 5.3 shows the power spectral density of the signals measured by the three barometers (shown in figure 5.1) between 0400 and 0600 EST on 18 Mar, 2008. The power spectral density was computed using the Welch's method of modified averaged periodogram with a Blackman window of 60 s width and 30 s overlap. A peak in the power spectral density can be observed at a frequency of about 0.18 Hz for all the three



**Figure 5.3.** Power spectral density of the data in figure 5.1. The RMS amplitudes of the microbaroms measured by the three barometers are 0.044236 Pa, 0.044163 Pa and 0.044580 Pa respectively.

signals, which falls in the microbarom frequency band. This affirms the detection of ocean generated infrasound (microbaroms) using a single absolute barometer. The RMS amplitude of the detected microbaroms was computed by integrating the power spectral density between 0.1 Hz (the trough) and 0.3 Hz and the values obtained are 0.044236 Pa, 0.044163 Pa and 0.044580 Pa respectively for the black, blue and red curves. The RMS amplitudes of the microbaroms detected by the three barometers are accurate down to few nanobars. The RMS amplitudes of the uncorrelated noise (estimated from the nearly flat asymptote at high frequencies) for a bandwidth of 1 Hz are 0.010564 Pa, 0.00966 Pa and 0.01242 Pa respectively. These values indicate the capability of these barometers to detect pressure fluctuations down to about fifty nanobars ( $0.05 \mu\text{bar}$ ). This detection amplitude of the barometer is about three times lower than the detection amplitude of a single sensor used in [20], the only reported detection of microbaroms using an array of absolute barometers. In fact, the detection amplitude of the barometer used here is about the same as the detection



**Figure 5.4.** Bandpass filtered time series of data in figure 5.1 for barometer #103946.

amplitude of the complete array of barometers (Model 216B-250 manufactured by Paroscientific, Inc.) used in [20].

Figure 5.4 shows the bandpass filtered time series of the data (red) in figure 5.1. A Blackman window was used and the lower and upper cut-off frequencies of the filter were 0.1 and 0.5 Hz respectively. Although the individual microbaroms cannot be resolved in the figure, temporal variations of the amplitude of the microbaroms can be observed from the envelope of the bandpass filtered microbaroms: oscillations of about 6 min periods can be seen between 0530 and 0600. The observed temporal variations can be attributed to the variations in temperature and wind of the upper atmosphere [12].

Figure 5.5 shows the zoomed-in pressure data over the boxed section of figure 5.1. The top plot is the actual zoomed-in section while the bottom plot is the mean removed version of the top plot. Microbaroms with peak amplitudes of less than 0.1

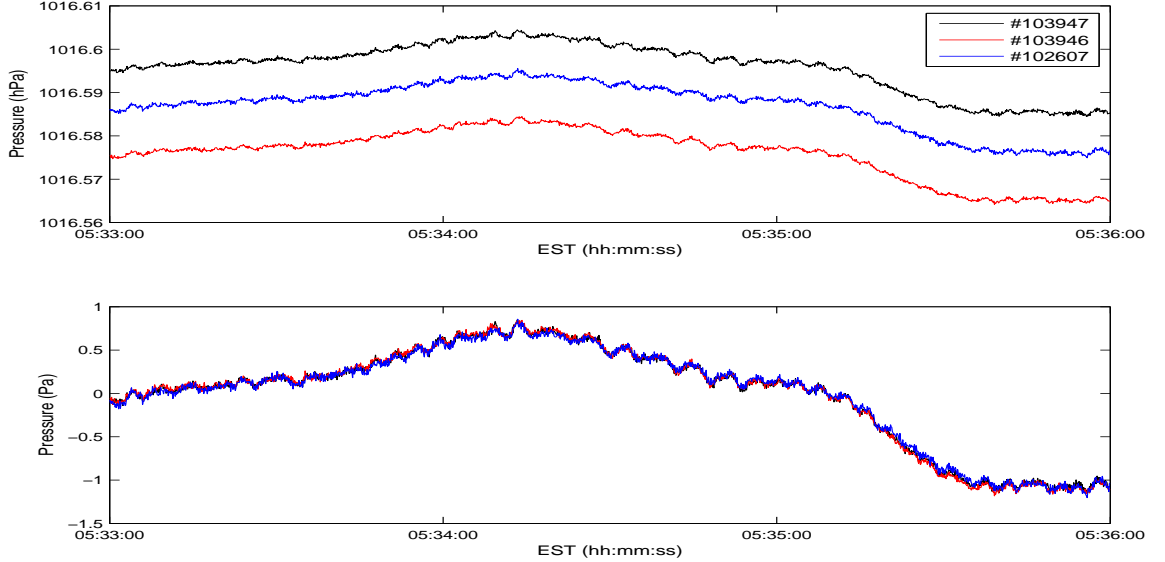


**Figure 5.5.** The data within the 3-min long time window indicated by the rectangle in figure 5.1. The top plot shows the actual data within the 3-min window. The bottom plot is the mean removed version of the top plot. Microbaroms with peak-to-peak amplitudes less than 0.1 Pa can be observed.

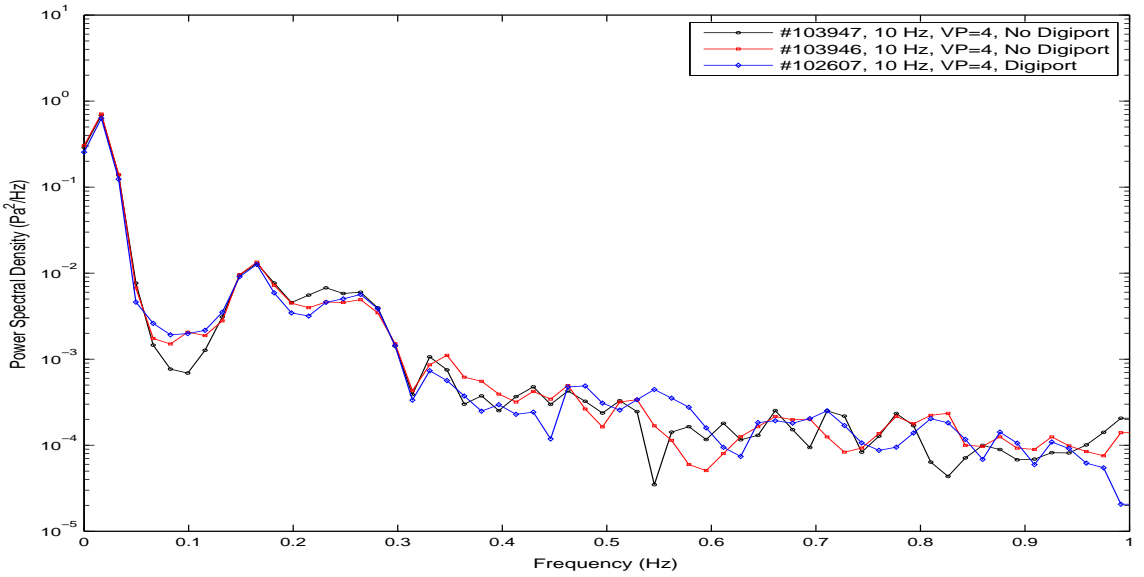
Pa can be observed in all the three time series (especially in the bottom plot). Figure 5.6 shows the power spectral density of the signals measured by the three barometers (shown in figure 5.5) between 0533 and 0536 EST on 18 Mar, 2008. Again, the Welch's method of modified averaged periodogram with a Blackman window of 60 s width and 30 s overlap was used. During this 3 min segment, two peaks in the power spectral density can be observed at about 0.17 Hz and 0.26 Hz respectively. This would mean that during this interval there were microbaroms detected from two different sources or there was some kind of frequency modulation of the microbaroms generated from a single source.

Figure 5.7 shows the bandpass filtered time series of the data in figure 5.5. A Blackman window was used and the lower and upper cut-off frequencies of the filter were 0.1 and 0.5 Hz respectively. Two microbarom periods of about 6.6 s and 3.7

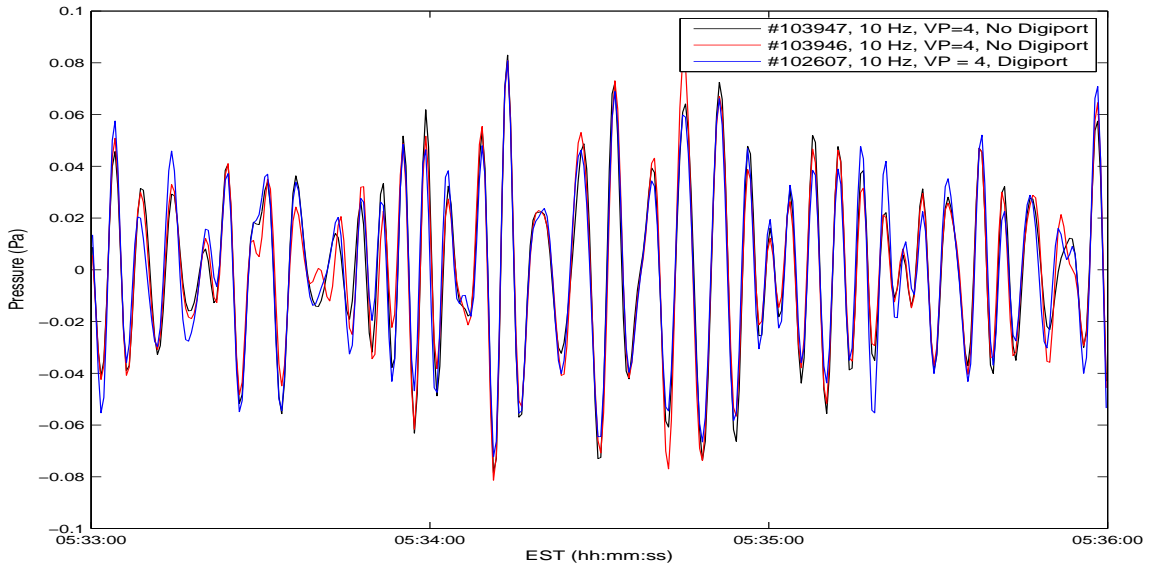
s can be observed as one would expect from the power spectral density (figure 5.6). Between 05:33:45 and 05:34:15 EST, approximately 3.7 s period microbaroms can be observed followed by 6.6 s period microbaroms until 05:34:55 EST. These time periods agree very well with the peak frequencies observed in the power spectral density (figure 5.6). It is apparent from the figure that microbaroms with the higher frequency have lower amplitudes than the microbaroms with the lower frequency. This observation is consistent with what we see in figure 5.6.

Figure 5.8 shows the time series of the difference between each pair of the signals shown in figure 5.5. The difference is nearly constant over the entire interval of 3 min which indicate that this was a relatively calm period. The mean values are 1.9980 Pa, -1.0946 Pa and -0.9034 Pa with standard deviations of 0.0193 Pa, 0.0348 Pa and 0.0270 Pa respectively for the black, red and blue curves.

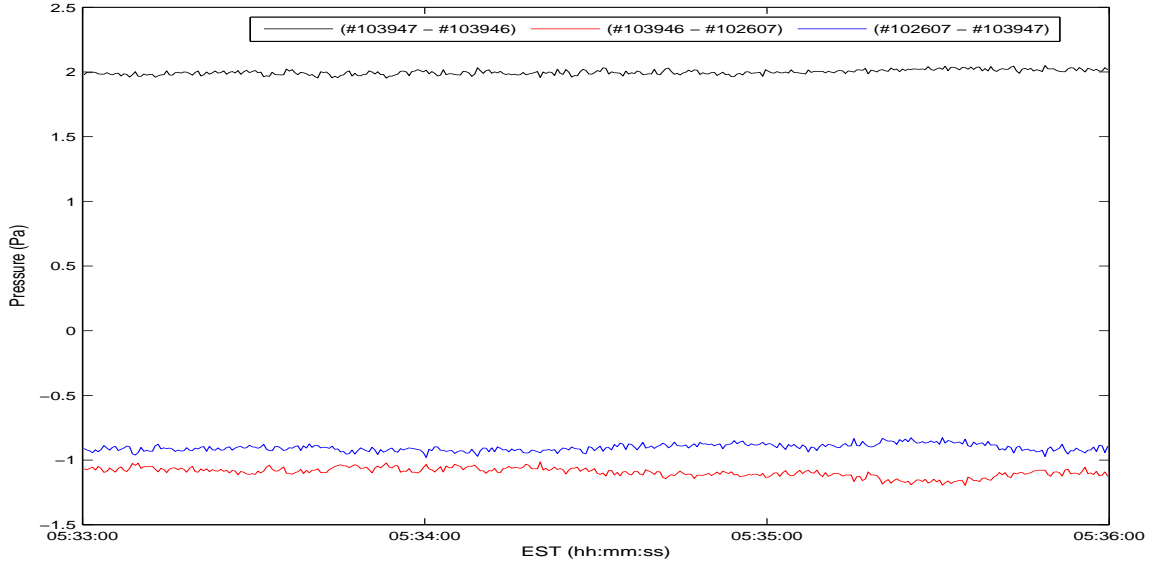
Figure 5.9 shows the time series of pressure measured by barometer #103947 from 1900 EST on 14 Mar, 2008 to 1900 EST on 20 Mar 2008 and figure 5.10 shows the spectrogram of the time series (in figure 5.9). For all spectrograms presented in this chapter, power spectral densities are computed over every successive 30 min periods using the Welch's method of modified averaged periodogram with a Blackman window of 60 s width and 30 s overlap, that is for each frequency there is one power spectral density estimate every 30 min. The colorbar in figure 5.10 shows the power spectral density values in dB. The data is normalized such that 0 dB corresponds to  $0.1 \text{ Pa}^2/\text{Hz}$ , that is deep red color in the spectrogram indicates highest intensity and deep blue color represents lowest intensity. Other colors, as indicated in the colorbar, represent the intensity between the two extremes. It can be observed that during the 15, 17 and 20 Mar (figure 5.9), pressure fluctuations with strong amplitudes occur. In general, high pressure areas are characterized by clear skies and calm weather while



**Figure 5.6.** Power spectral density of the data in figure 5.5. The RMS amplitudes of the microbaroms measured by the three barometers are 0.047616 Pa, 0.045430 Pa and 0.044709 Pa respectively. There are two microbarom peaks which could be due to frequency modulation of the microbarom frequency or due to microbaroms from two different sources.



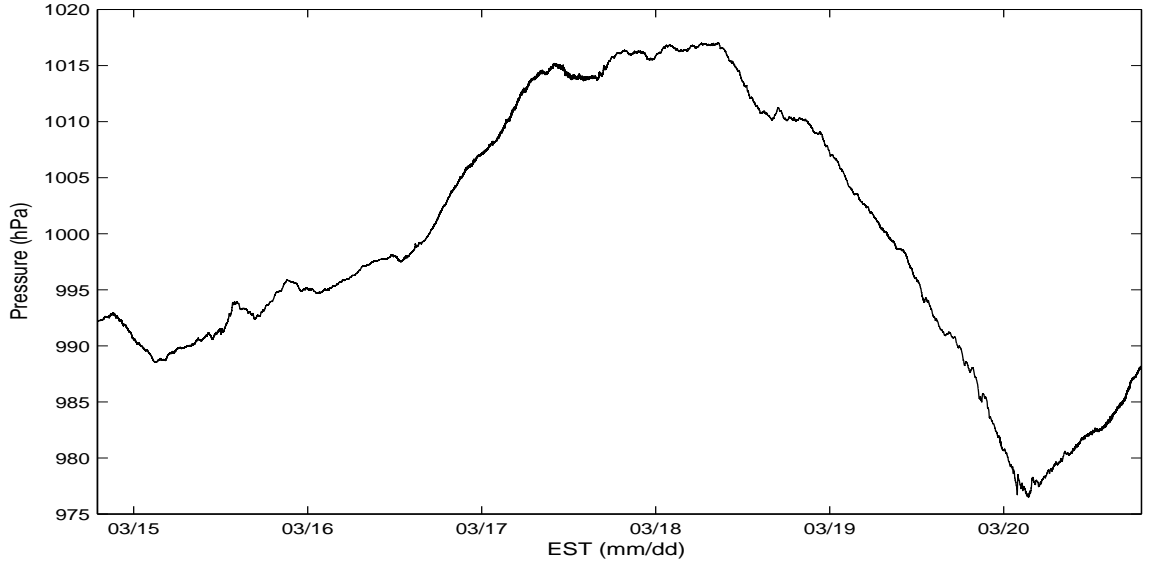
**Figure 5.7.** Bandpass filtered time series of data in figure 5.5. Two microbarom time periods of about 6.6 s and 3.7 s can be observed which is expected from figure 5.6. Also the three time series track each other very closely.



**Figure 5.8.** Time series of the difference between the three signals of figure 5.5. The mean values are 1.9980 Pa, -1.0946 Pa and -0.9034 Pa with standard deviations of 0.0193 Pa, 0.0348 Pa and 0.0270 Pa respectively.

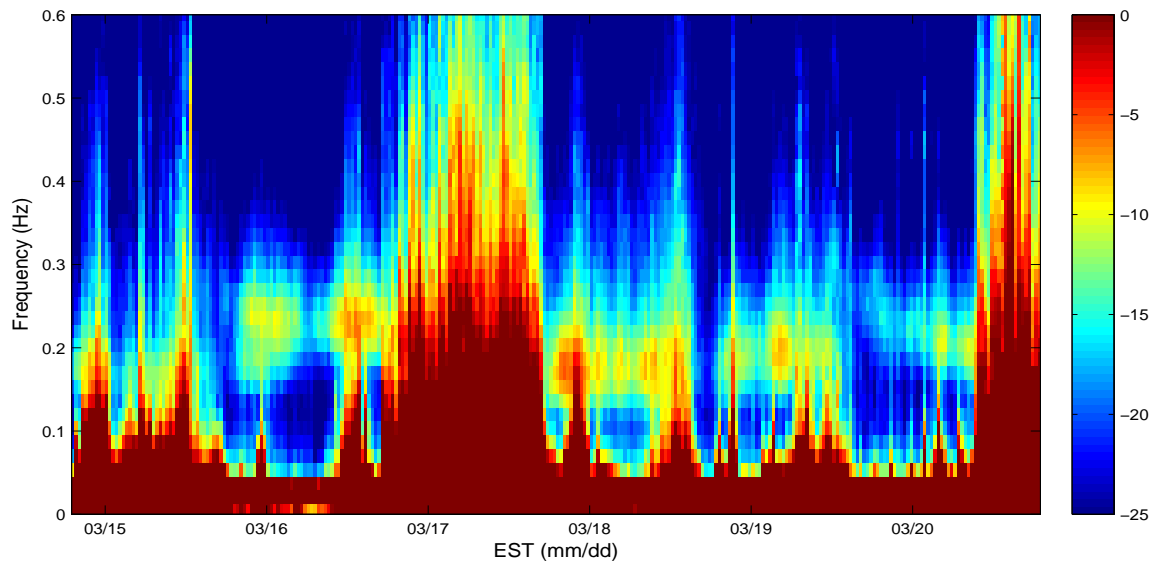
low pressure areas are characterized by stormy weather. Hence, from figure 5.9, one would expect stormy weather on the 15 and 20 Mar. This is exactly what the spectrogram in figure 5.10 indicates, where in high intensity pressure fluctuations can be seen up to 0.25 Hz on the 15<sup>th</sup> and 1 Hz on the 20<sup>th</sup>. During the 17<sup>th</sup>, although there is no observation of low pressure (figure 5.9), there are strong pressure fluctuations observed which are due to strong winds. This is also consistent with the observations from the spectrogram in figure 5.10. Such stormy periods obscure the microbaroms in the data. Even though figure 5.10 indicates that the storm during the 15<sup>th</sup> was not as intense as the one during the 20<sup>th</sup>, it is strong enough to obscure the observation of microbaroms.

Figure 5.11 shows the horizontal wind speed time series from 1900 EST on 14 Mar, 2008 to 1900 EST on 20 Mar 2008. The 32 Hz anemometer data has been averaged over 30 min intervals such that there is one data point every 30 min. The mean



**Figure 5.9.** The raw pressure time series between 1900 EST on 14 Mar and 1900 EST on 20 Mar 2008.

horizontal wind speeds during the stormy periods on the 15<sup>th</sup>, 17<sup>th</sup> and 20<sup>th</sup> were 0.5287 ms<sup>-1</sup>, 0.7812 ms<sup>-1</sup> and 0.7716 ms<sup>-1</sup> respectively. These winds with relatively high mean wind speed (Note: These winds were measured on the ground next to the trailer, which was located in a wooded area.) induce pressure fluctuations that are broad band and strong enough to obscure the microbaroms. During the rest of the periods, when the horizontal wind speed is less than 0.5 ms<sup>-1</sup>, microbaroms can be observed clearly as a peak in the intensity around 0.2 Hz. The temporal amplitude variations of the microbaroms can be seen from the spectrogram with the microbaroms showing up in different colors from orange down to light blue. The temporal variation in frequency of the microbaroms can also be observed from the spectrogram. Analysis and interpretation of the temporal variations of the frequency and amplitude of the microbaroms will be presented in the next section.



**Figure 5.10.** Spectrogram of data in figure 5.9. The colorbar shows the power spectral density values in dB. The data is normalized such that 0 dB corresponds to  $0.1 \text{ Pa}^2/\text{Hz}$ . Strong microbaroms are observed and the observations are consistent with the raw data in figure 5.9.

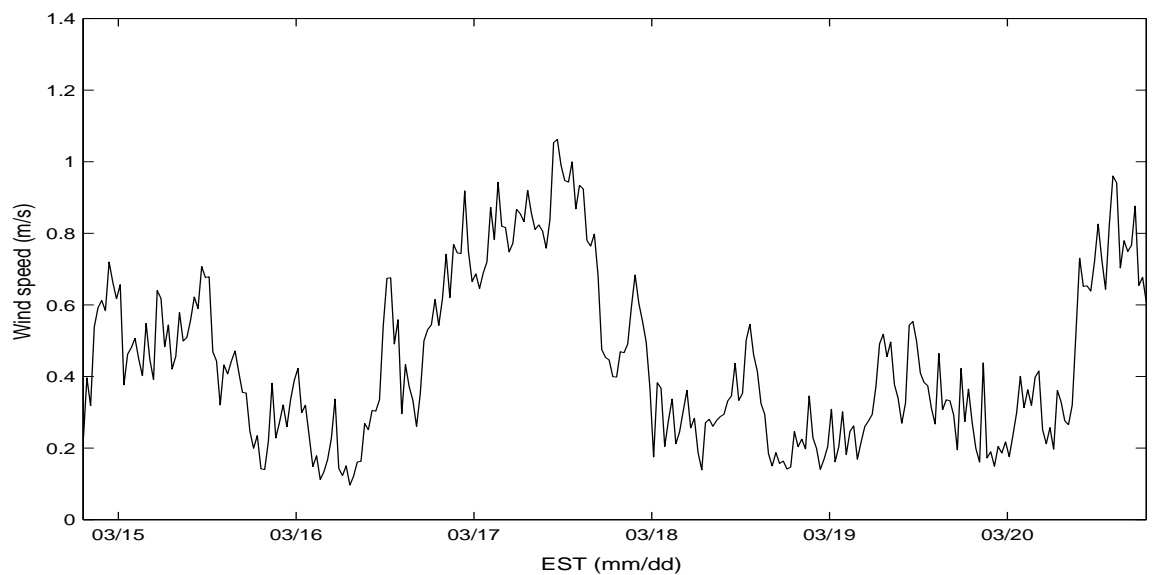


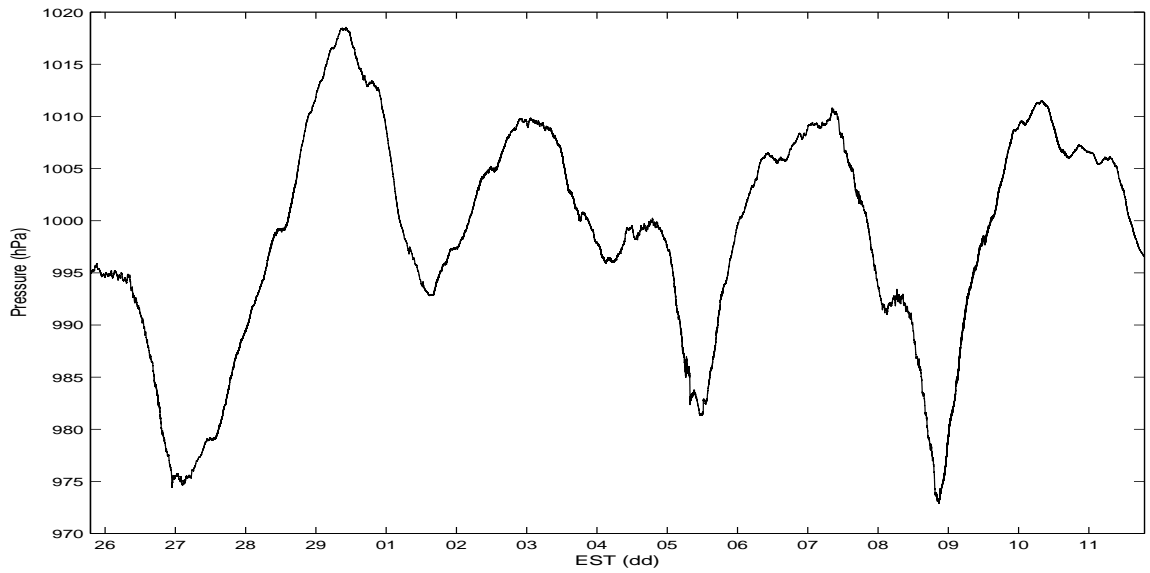
**Figure 5.11.** Horizontal wind speed time series between 1900 EST on 14 Mar and 1900 EST on 20 Mar 2008.

## 5.2 Temporal Variations of the Amplitude and Frequency of the Microbaroms

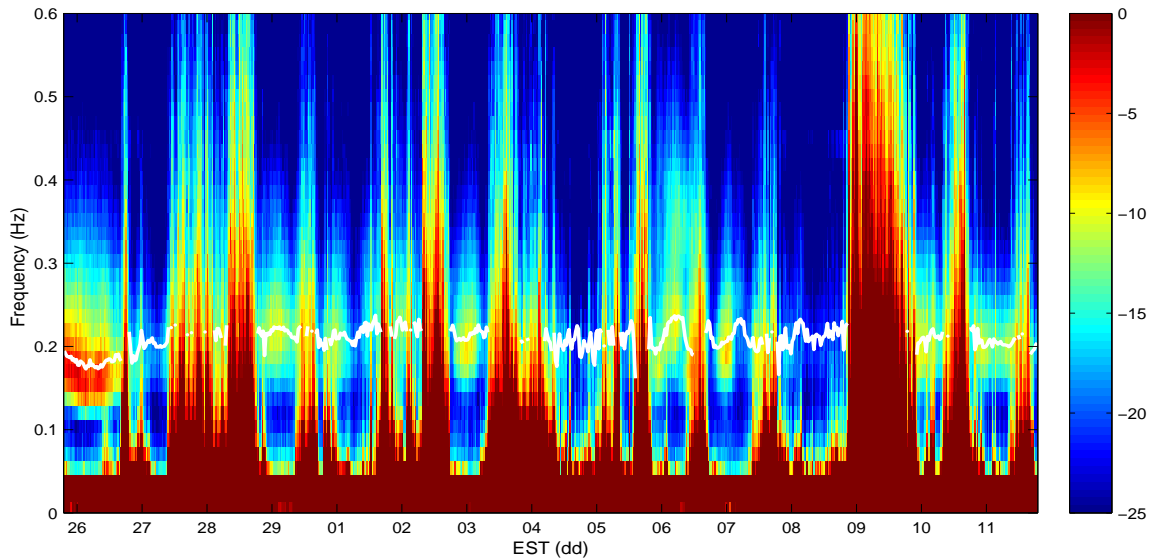
In the previous section, especially in figure 5.10, the temporal variations in frequency and amplitude of the microbaroms are evident. In this section, an attempt is made to interpret such observed temporal variations.

Figure 5.12 shows the time series of pressure measured by barometer #103947 from 1900 EST on 25 Feb, 2008 to 1900 EST on 11 Mar 2008. The tick marks on the *x axis* denote the beginning of a day. From Fig 5.12 one would expect stormy and windy conditions (thunderstorms) during the low pressure periods on the 27<sup>th</sup>, 28<sup>th</sup> 5<sup>th</sup> and the 9<sup>th</sup>. It is also expected, from figure 5.12, that strong winds would have prevailed during parts of the 2<sup>nd</sup>, 3<sup>rd</sup>, 4<sup>th</sup>, 6<sup>th</sup>, 7<sup>th</sup> and the 11<sup>th</sup> since we have significant changes in pressure during these periods. This can be confirmed from figures 5.13 and 5.14. Figure 5.13 shows the spectrogram of the time series (in figure 5.12). As before, the spectrogram is normalized such that 0 dB corresponds to a power spectral density value of  $0.1 \text{ Pa}^2/\text{Hz}$ . The time series of the centroid frequency of the microbaroms, computed as explained in section 4.5, is plotted (in white) over the spectrogram in figure 5.13. Figure 5.14 shows the time series of horizontal wind speed during the same time period. Microbaroms can be observed from the spectrogram during periods where there was relatively constant pressure (changes of a few hPa) and low wind speeds. In fact, no microbaroms are observed when the horizontal wind speed exceeds  $0.5 \text{ ms}^{-1}$ . It is evident, from this spectrogram (figure 5.13) also, that there are temporal variations in the frequency and amplitude of the microbaroms.

In order to explain the temporal variation of the frequency of the microbaroms, the wind speed time series (figure 5.14) is analyzed and related to the centroid frequency in the spectrogram (figure 5.13). Usually during periods of strong winds we



**Figure 5.12.** Raw pressure time series between 26 Feb and 11 Mar 2008.



**Figure 5.13.** Spectrogram of data in figure 5.12 with the centroid frequency. The Colorbar shows the PSD values in dB. The data is normalized such that 0 dB corresponds to  $0.1 \text{ Pa}^2/\text{Hz}$ . The observations are consistent with figure 5.12 and also the centroid frequency agrees very well with the spectrogram.

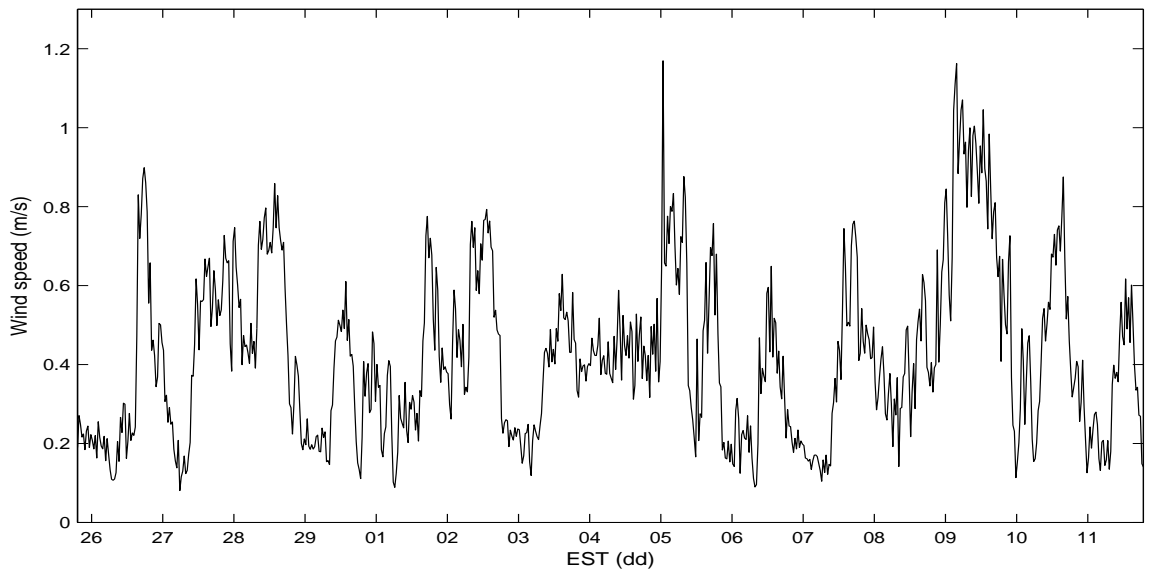


**Figure 5.14.** Horizontal wind speed time series between 1900 EST on 25 Feb and 1900 EST on 11 Mar 2008.

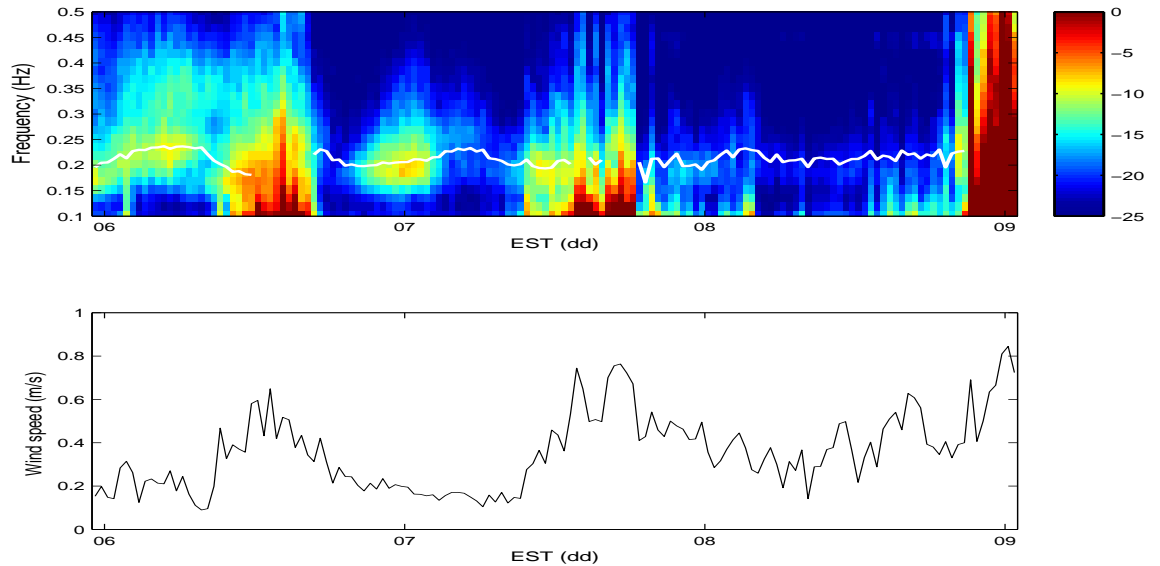


**Figure 5.15.** Zoomed-in segment of figures 5.13 and 5.14 between 06 Mar and 09 Mar 2008. There seems be a very nice inverse relationship between the wind speed and the microbarom centroid frequency.

have longer waves than during the calm periods. Thus during periods of strong winds the frequency of the microbaroms should be less than the frequency of microbaroms during calm periods. This fact is consistent with the observations from figures 5.13 and 5.14: there is an inverse relationship between the wind speed and the microbarom frequency. To support the observation, we zoom in to a 3 days segment, between 06 Mar and 09 Mar 2008, of figures 5.13 and 5.14 (shown in figure 5.15). The *y axis* of the spectrogram (top plot) has been limited between 0.1 Hz and 0.4 Hz. It is quite obvious that there is no observation of microbaroms when the wind speed exceeds  $0.5 \text{ ms}^{-1}$ . Just before noon on the 6<sup>th</sup>, when the wind speed rapidly increases, a rapid decrease in the microbarom frequency can be observed. Again during the morning of the 7<sup>th</sup>, when the wind speed reaches its minimum value, the microbarom frequency reaches its maximum. Thus, there is an obvious inverse relationship between the horizontal wind speed and the microbarom frequency over significant periods of time, if not always.

Figure 5.16 shows the time series of microbarom RMS amplitude between 1900 EST on 25 Feb and 1900 EST on 11 Mar 2008. The amplitudes are computed over non-overlapping 30 min segments using the algorithm described in section 4.5. The black curve in the top plot represents the amplitude computed within a constant frequency band (0.1 - 0.3 Hz) irrespective of whether microbaroms are detected or not. The red curve represents the amplitude computed, only when microbaroms are detected, within an adaptive frequency band (section 4.5) with its upper cut-off frequency fixed at 0.3 Hz. The bottom plot shows only the RMS amplitude computed using the adaptive algorithm. The amplitudes are consistent with the observations from figure 5.13. Also, the two time series track each other very closely during periods when microbaroms are actually detected. A semidiurnal (period of 12 h) variation in amplitude (red curve) can be seen on the 7<sup>th</sup> and 11<sup>th</sup> in figure 5.16 which may

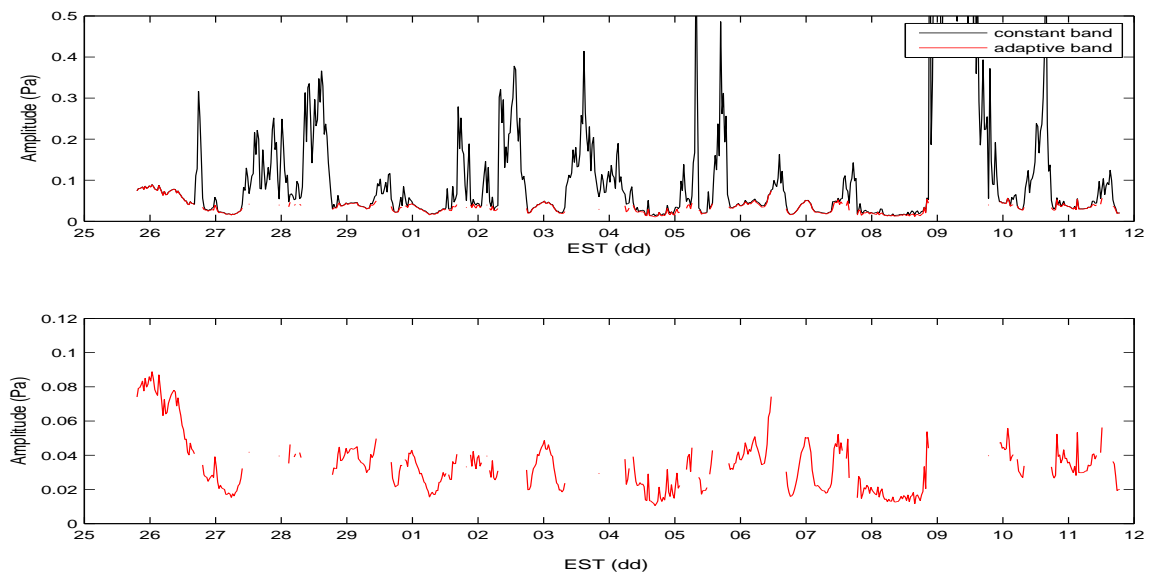


**Figure 5.16.** Microbarom amplitude time series of data in figure 5.12. The observations are consistent with figure 5.13. The amplitude computed within the adaptive frequency band has 'NaN' values when no microbaroms are observed.

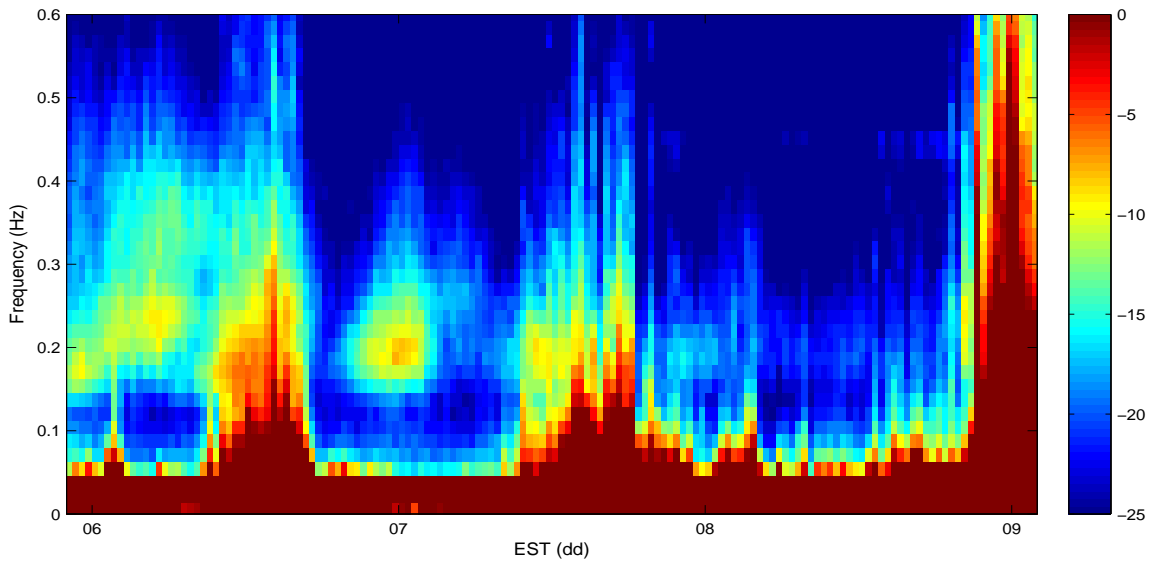


**Figure 5.17.** Zoomed-in version of the spectrogram in figure 5.12.

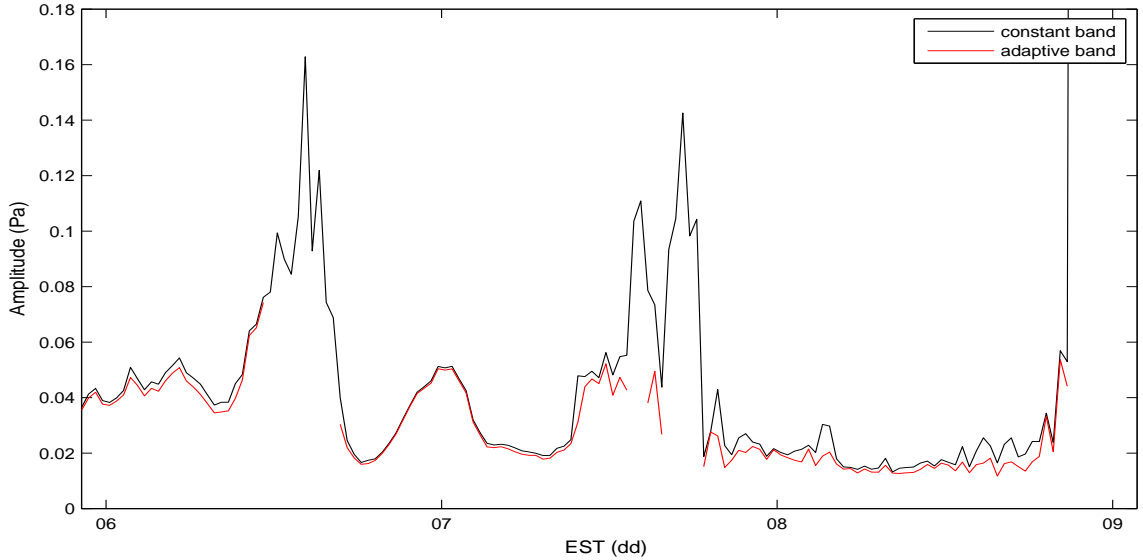


**Figure 5.18.** Zoomed-in version of microbarom amplitude time series of figure 5.16 corresponding to figure 5.17. The observations agree very well with that of figure 5.17.

be attributed to the semidiurnal atmospheric tides in the upper atmosphere. Figures 5.17 and 5.18 shows the segment between 06 and 09 Mar, 2008, of figures 5.13 and 5.16 respectively. The peak amplitude of the microbaroms observed in figure 5.18 around the beginning of 7 Mar, 2008 can be noticed in figure 5.17 as well. The power spectral density value changes in color from light blue (minimum) to orange (at the peak during the beginning of 7<sup>th</sup>) and shifts gradually back to light blue. The decreasing amplitude early in the morning of the 8<sup>th</sup> is observed in both figures 5.17 and 5.18. Thus, the microbarom amplitude time series is consistent with the spectrogram.

The explanation of the observed temporal variations in the amplitude of the microbaroms has been adapted from [12], assuming that the source intensity is constant. Microbaroms are sound waves that propagate at the speed of sound. These waves propagate through waveguides (sound channels) created in the atmosphere. At any height above ground, the effective speed of sound is a function of both the temperature

and wind. As we move up from the surface to the upper atmosphere strong vertical gradients of temperature and wind may exist. Some level in the upper atmosphere, where the speed of sound matches with the speed of sound at the ground, acts as the upper boundary for the sound duct (the lower boundary being the ground). When the microbaroms are radiated by the ocean in all directions (predominantly in the vertical), these waves get reflected back and forth between the two boundaries of the sound channel, when the incident angle is greater than the critical angle. Thus, different points on the ground receive the microbaroms after one or more upper boundary reflections.

Microbaroms undergo some loss in intensity as they propagate through the atmosphere. The higher the altitude of the upper boundary of the sound channel, the greater will be the viscous damping and hence the greater will be the loss in intensity of the microbaroms. The temporal variation in the amplitude of the microbaroms can be attributed to the temporal variation in the altitude of the upper boundary of the sound channel. On the basis of temperature alone, the upper boundary of the sound channel is at about 110 km (Fig 2 of [12]). Short-term temperature and wind fluctuations may cause the altitude of the upper reflection boundary layer to change significantly. Such temperature and wind fluctuations in the upper atmosphere are affected by factors like the prevailing winds (depends on the season), atmospheric tides and gravity waves. In order to understand the temporal variations of the amplitude of the microbaroms, it is very important to know the temperature and wind field structure of the upper atmosphere.

Figures 5.19 and 5.20 confirm the effectiveness of the adaptive algorithm used to compute the microbarom centroid frequency and amplitude. Figure 5.19 shows no presence of microbaroms and hence the algorithm assigns NaN (Not a Number)

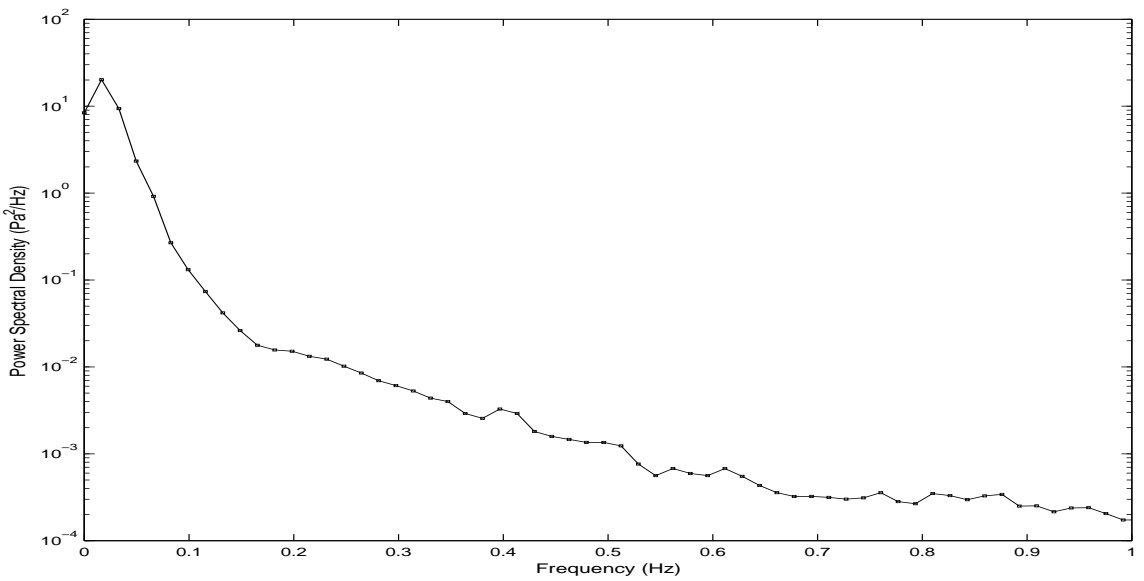


**Figure 5.19.** Power spectral density of barometer #103946 between 1430 and 1500 EST on 06 Mar 2008. Since no microbaroms are observed, the value 'NaN' is assigned to the microbarom amplitude which can be seen in Fig 5.18.

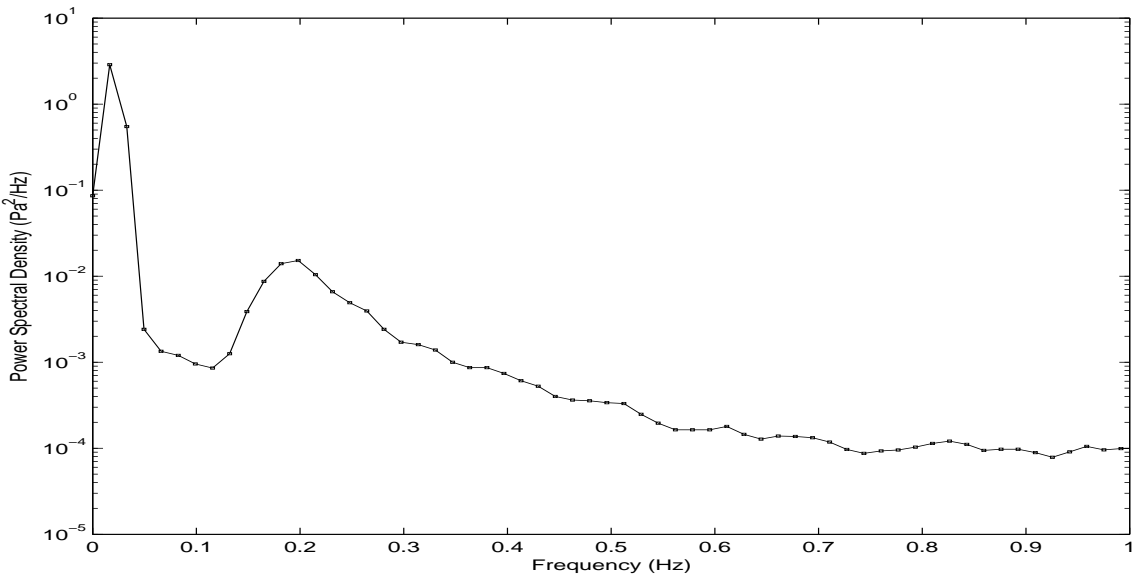


**Figure 5.20.** Power spectral density of barometer #103946 between 0000 and 0030 EST on 07 Mar 2008. Since microbaroms are observed, the microbarom amplitude is computed which can be seen in Fig 5.18.

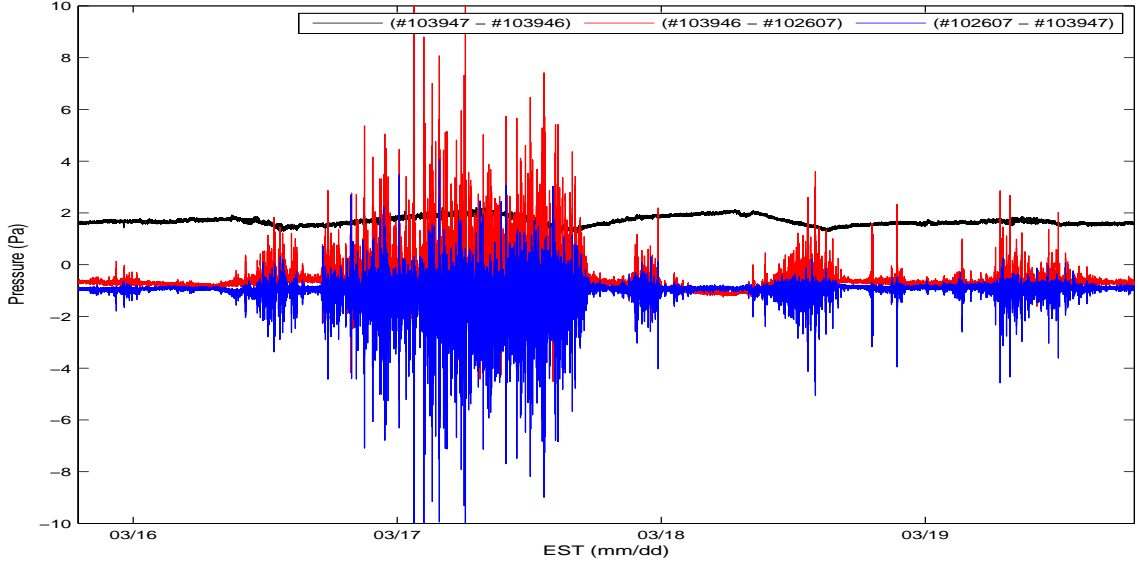


**Figure 5.21.** Time series of the difference between the three signals between 1900 EST on 15 Mar, 2008 and 1900 EST on 19 Mar, 2008. The mean values are 1.6894 Pa, -0.7242 Pa and -0.9652 Pa with standard deviations of 0.1654 Pa, 0.2958 Pa and 0.2742 Pa respectively.

values to the microbarom frequency and amplitude (shown in figures 5.18 and 5.15). Alternatively, figure 5.20 shows the presence of microbaroms and hence the algorithm computes the amplitude and frequency of the microbaroms (figures 5.18 and 5.15) which are consistent with the observations from the spectrogram (figure 5.17) and the power spectral density (figure 5.20).

### 5.3 Performance of the Barometers and the DigiPort

In this section, results that describe overall performance of the barometers will be presented and interpreted.

To estimate the relative error in measurement between the barometers and to observe its variation with time (large-scales), if any, the time series of the difference

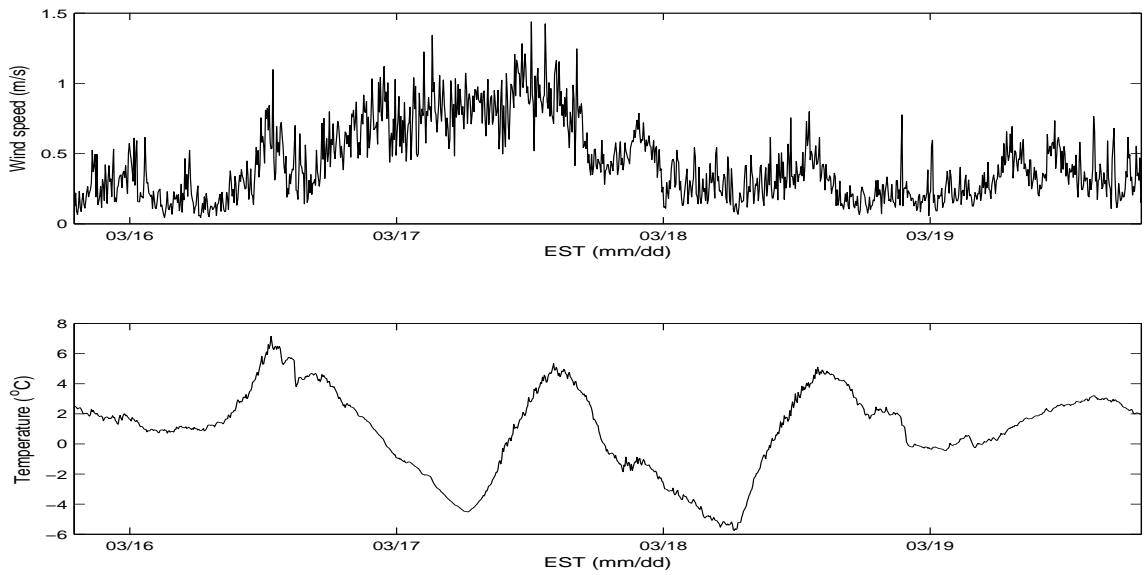


**Figure 5.22.** Horizontal wind speed and temperature time series between 1900 EST on 15 Mar, 2008 and 1900 EST on 19 Mar, 2008.

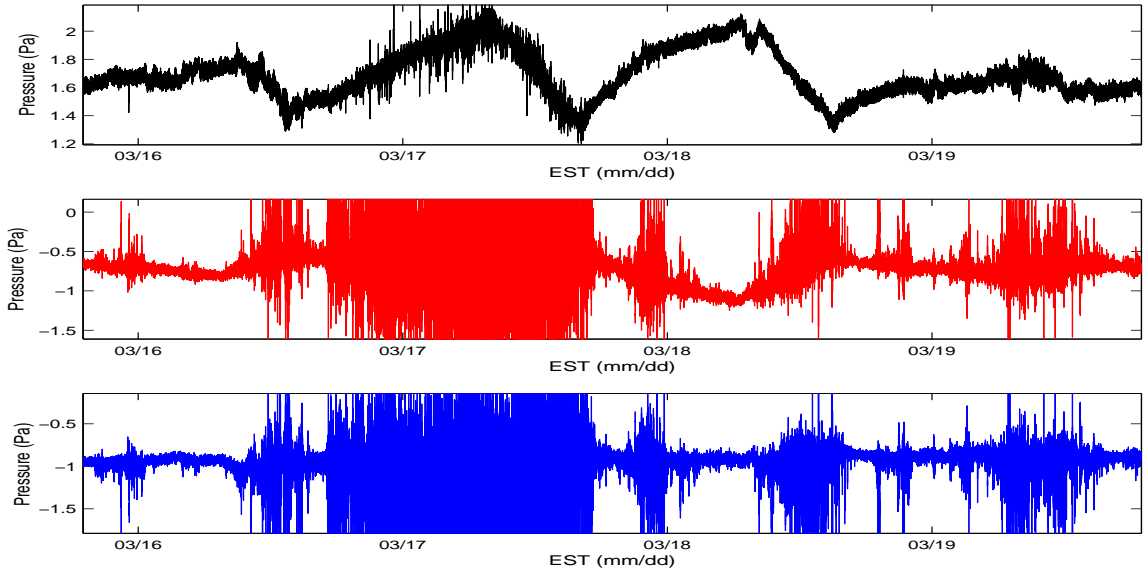


**Figure 5.23.** Time series of figure 5.21 shown in three separate subplots. For each subplot, the y-axis is limited between  $\pm 3\sigma$  from the respective mean values. Legends are the same as in figure 5.21.

between the three pairs of barometers is shown in figure 5.21. The mean values of the black, red and blue curves are 1.6894 Pa, -0.7242 Pa and -0.9652 Pa with standard deviations of 0.1654 Pa, 0.2958 Pa and 0.2742 Pa respectively. Figure 5.22 shows the wind and temperature time series during the same time range as figure 5.21. It is evident that during periods of strong winds, the fluctuations of the red and blue curves in figure 5.21 have greater amplitudes than the black curve, which is expected considering the fact that the two barometers without the DigiPort measure the pressure inside the trailer while the barometer with the DigiPort measures the pressure outside the trailer. Figure 5.23 shows the three time series of figure 5.21 in three separate subplots. For each subplot, the *y axis* has been limited between  $\pm 3\sigma$  from the respective mean values. The black and red curves show similar, but with different sign, changes over time scales of the order of few hours while the blue curve appears to be fairly constant over the exact same time scales. These changes are strongly related to the changes in temperature shown in figure 5.22. It can be seen that the red and black curves reach their minimum and maximum respectively when the temperature reaches its minimum (early morning of 18 Mar). Also, when the temperature reaches its maximum after noon on the 18<sup>th</sup>, the black and red curves reach their minimum and maximum respectively. This implies that there was something partially or completely wrong with the temperature compensation of the barometer #103946.

Random errors [28] are always present in a measurement system and cannot be eliminated. While random errors are unpredictable, systematic errors are predictable. Systematic errors [28] in a measurement system are mostly constant or proportional to the true value being measured and are usually caused by imperfect calibration of measurement instruments. Small systematic errors are inherent to almost all measurement systems. Thus, the sources of the random errors in the measurement of pressure using these barometers are the wind and temperature (when temperature

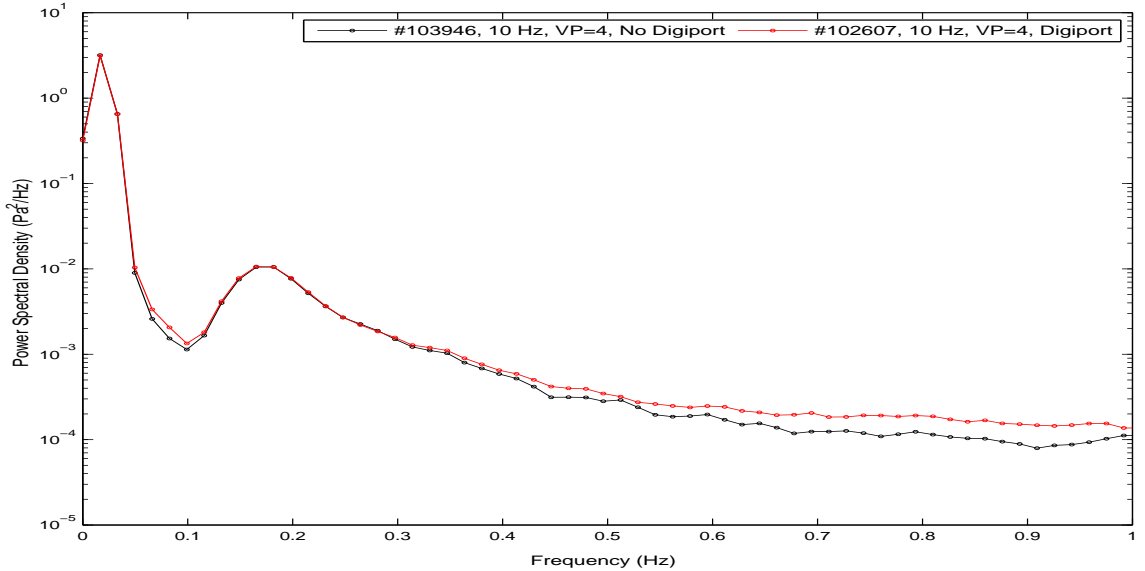


**Figure 5.24.** Power spectral density between 0400 and 0600 EST on 18 Mar 2008. The mean wind speed during this period is 0.3013 m/s. The barometer with the DigiPort has a detection amplitude of 0.012425 Pa while the barometer without DigiPort has a detection amplitude of 0.010124 Pa.

compensation goes wrong). The observed mean values of the difference between the signals measured by each pair of barometers can be attributed to the systematic errors inherent to the barometers. It can be concluded from figure 5.21 that the relative error in measurement (random and systematic) between these barometers is of the order of a few pascals (few tens of a microbar).

To study the effectiveness of the DigiPort that is expected to reduce wind induced pressure fluctuations considerably, power spectral density is computed during one calm and one stormy period of time. Figure 5.24 shows the power spectral density of the signals measured, by the barometers with and without the DigiPort, during the interval between 0400 and 0600 EST on 18 Mar 2008 when the mean wind speed was  $0.3013 \text{ ms}^{-1}$ . It can be seen that the barometer with the DigiPort (red curve) has a higher detection amplitude than the barometer without the DigiPort (black curve).

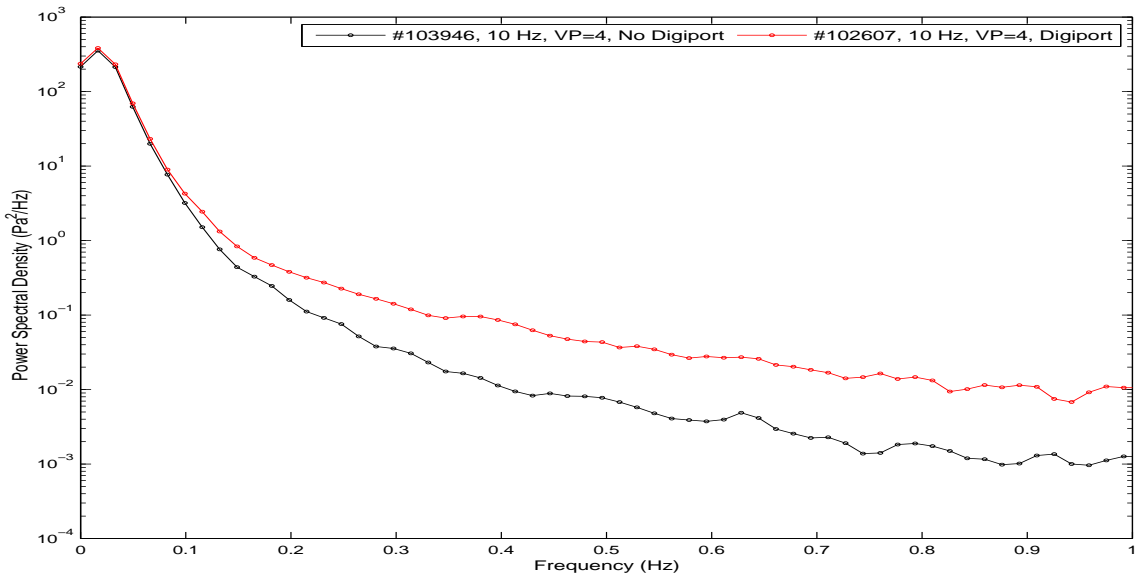


**Figure 5.25.** Power spectral density between 1200 and 1400 EST on 17 Mar 2008. The mean wind speed during this period is 1.0391 m/s. The barometer with the DigiPort has a detection amplitude of 0.09585 Pa while the barometer without DigiPort has a detection amplitude of 0.03104 Pa.

The values are 0.012425 Pa and 0.010124 Pa respectively for the red and black curves.

Fig 5.25 shows the power spectral density of the signals measured, by the barometers with and without the DigiPort, during the interval between 1200 and 1400 EST on 17 Mar 2008 when the mean wind speed was  $1.0391 \text{ ms}^{-1}$ . It can be seen that the barometer with the DigiPort (red curve) has a much greater detection amplitude than the barometer without the DigiPort (black curve). The values are 0.09585 Pa and 0.031041 Pa respectively for the red and black curves. Thus, it is clear that the detection amplitude increases as the wind speed increases, for both the barometers, which is as expected.

To illustrate the variation of detection amplitude ("noise floor") with wind speed over a longer time range, Figure 5.26 is presented which shows the spectrogram of

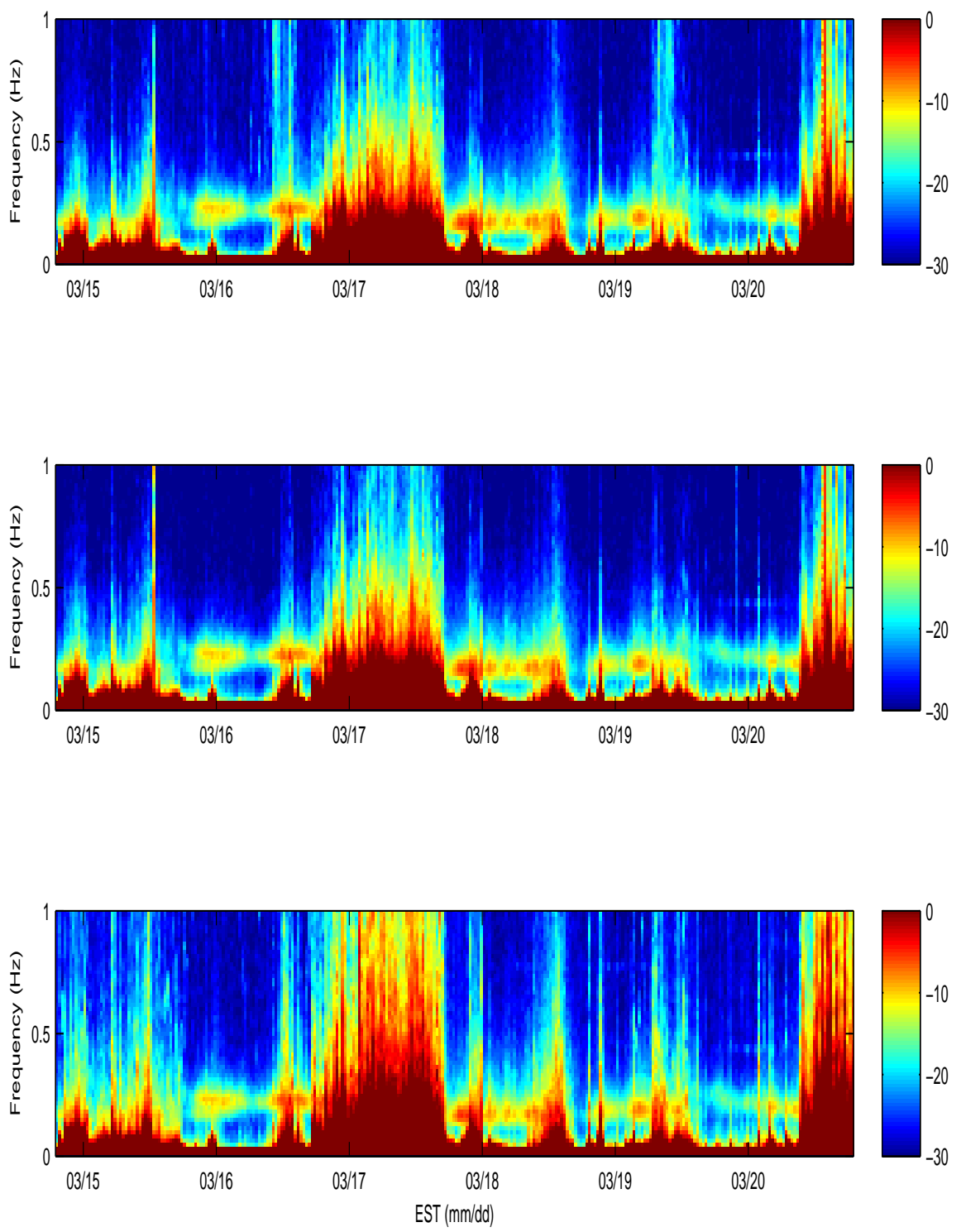
the signals measured by the three barometers between 1900 EST on 14 Mar, 2008 and 1900 EST on 20 Mar, 2008. The top plot is for barometer 103947 (no DigiPort), the middle plot is for barometer #103946 (no DigiPort) and the bottom plot is for barometer #102607 (with DigiPort). The spectrograms are normalized such that 0 dB maps to  $0.1 \text{ Pa}^2/\text{Hz}$ . It is clear that during periods of strong winds, especially the 17<sup>th</sup> and the 20<sup>th</sup> (figure 5.22), we see relatively higher noise floor (for all three barometers) than the rest of the periods. Another important observation from figure 5.26 is that the barometer with the DigiPort (bottom plot), in general, has a higher noise floor than the other two. Also during windy conditions (especially on the 17<sup>th</sup> and the 20<sup>th</sup>), the barometer with the DigiPort (bottom plot) has a much greater noise floor than the other two barometers. For instance, on the 17<sup>th</sup> the barometer with the DigiPort has a noise floor of approximately 0.095 Pa while the other two barometers have noise floors of about 0.035 Pa each. This implies that the travel trailer, owing to its much larger size than the DigiPort, reduces wind induced pressure fluctuations better. The previous statement assumes that the addition of a DigiPort would make the barometer less susceptible to wind induced pressure fluctuations than a naked barometer installed outside the travel trailer, that is the DigiPort indeed helps reduce wind induced pressure fluctuations.

It can also be seen (in Fig 5.26), that the two barometers without the DigiPort themselves, at times, have significantly different noise floors. For instance, before noon on the 19<sup>th</sup> the noise floor of barometer #103947 is nearer to the noise floor of barometer #102607 (with DigiPort) than the barometer 103946. Such a significant difference in the noise floors between the two barometers inside the travel trailer could possibly be due to the individual locations of the barometers inside the trailer. Although the barometers were placed only a few centimeters apart on a table (near a window) inside the trailer, it is possible that the two barometers were placed such

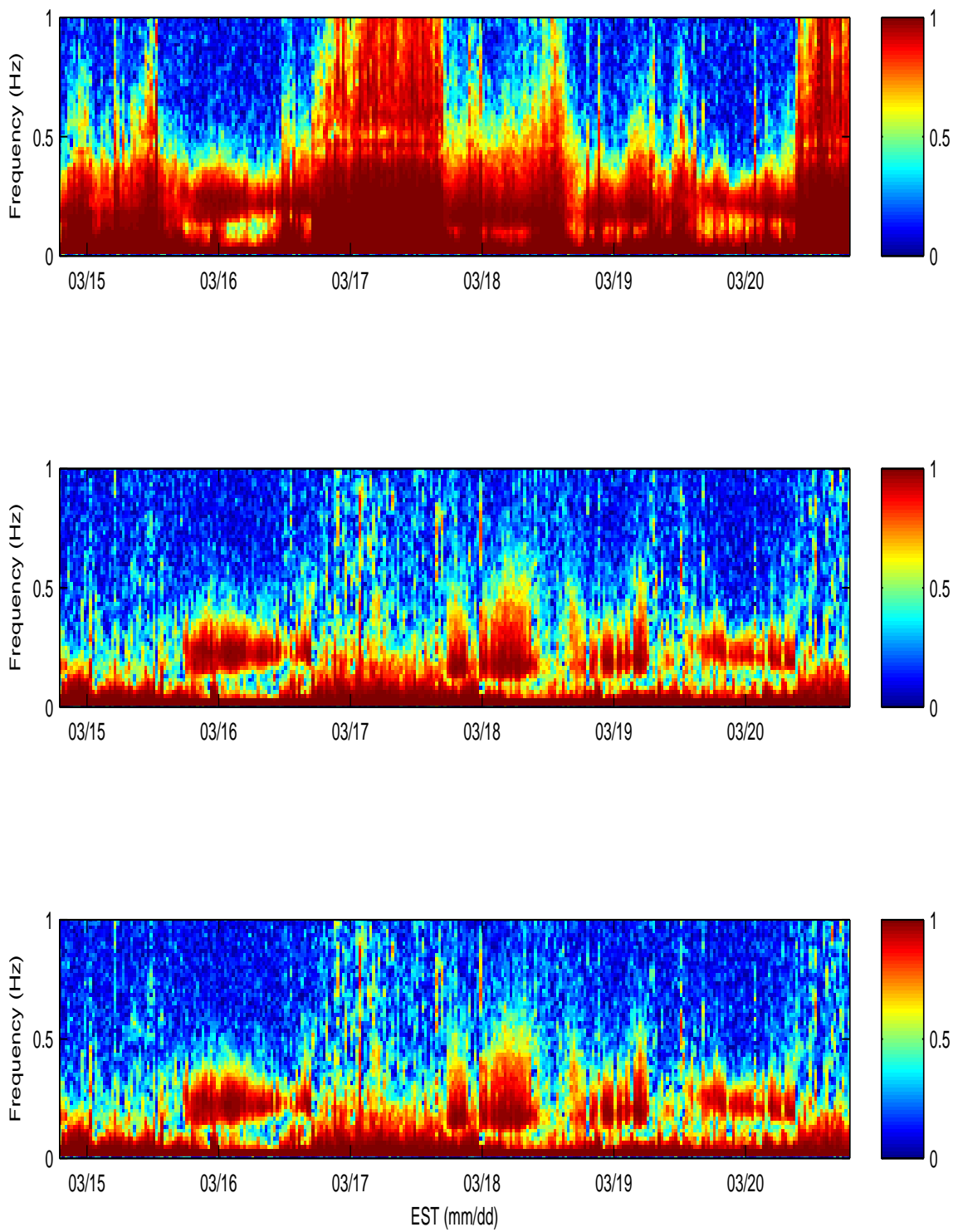
that one was closer to the window than the other, which could mean that the one closer to the window would have a higher noise floor. Another plausible situation would be that the two barometers were placed near the two ends of the window and that the direction of the wind accounts for the different noise floors observed. Further research needs to be carried out to arrive at a conclusion as to what causes the significant differences in noise floor between the two barometers inside the travel trailer.

Figure 5.27 shows the coherence spectrogram between the signals measured by the three barometers between 1900 EST on 14 Mar, 2008 and 1900 EST on 20 Mar, 2008. The top plot is for the barometer pair #103947 (no DigiPort) and #103946 (no DigiPort), the middle plot is for the barometer pair #103946 (no DigiPort) and #102607 (with DigiPort), and the bottom plot is for the barometer pair #102607 (with DigiPort) and #103947 (no DigiPort). The colorbar represents the values of the coherence spectrum (between 0 and 1). It is clear that during the periods of strong winds (esp. 17<sup>th</sup> and 19<sup>th</sup>), the coherence between signals measured by the barometer with the DigiPort and the barometer without the DigiPort falls below 0.4 for frequencies above 0.4 Hz (middle and bottom plots). This again implies that the travel trailer filters out the wind induced pressure fluctuations better than the DigiPort. During calm periods, when microbaroms are detected, the peak in coherence between each pair of signals show up in deep red color in the microbarom frequency band (all three plots). Also, during windy periods, the fact that there is very high coherence up to 0.5 Hz between the signals measured by the two barometers without the DigiPort (top plot), confirms that the trailer does not filter out the wind induced pressure fluctuations completely.

The travel trailer filters out a significant portion of the wind induced pressure fluctuations (middle and bottom plot) at frequencies greater than 0.1 Hz during the



**Figure 5.26.** Spectrogram of the signals measured by the three barometers between 1900 EST on 14 Mar, 2008 and 1900 EST on 20 Mar, 2008: Top plot is for barometer #103947 (no DigiPort), the middle plot is for barometer #103946 (no DigiPort) and the bottom plot is for barometer #102607 (with DigiPort).



**Figure 5.27.** Coherence spectrogram between the signals measured by the three barometers between 1900 EST on 14 Mar, 2008 and 1900 EST on 20 Mar, 2008: Top plot is for the barometer pair #103947 (no DigiPort) and #103946 (no DigiPort), the middle plot is for the barometer pair #103946 (no DigiPort) and #102607 (with DigiPort), and the bottom plot is for the barometer pair #102607 (with digiport) and #103947 (no DigiPort).

early hours of 19<sup>th</sup>, however there is no indication of a peak in coherence showing the presence of microbaroms. This means that, microbaroms either do not reach the ground, due to elevation of the waveguide through which they propagate [12], or they are completely obscured by the strong winds.

Thus, to summarize the performance of the barometers and DigiPort, the relative error in measurement between two barometers placed a few centimeters apart is of the order of a few pascals (few tenths of a microbar). The noise floor (detection limit) of the barometer with the digiport ranges approximately between 0.1 microbars during calm conditions and about 1 microbar during stormy conditions. The noise floor of the naked barometers placed inside the travel trailer ranges approximately between 0.1 microbars during calm conditions and about 0.4 microbar during stormy conditions. Thus, the travel trailer provides a better shield from wind induced pressure fluctuations. The detection limit of both, the barometer with the DigiPort and the naked barometer inside the trailer, is approximately 0.1 microbars during calm weather conditions. Hence for the purpose of detection of microbaroms during relatively calm weather, which is the only condition during which these barometers have detected microbaroms, the choice of using a barometer with DigiPort or a naked barometer inside a closed structure (like the trailer) is insignificant.

## CHAPTER 6

### CONCLUSIONS AND DISCUSSIONS

In this chapter, the important results from the previous section are listed and then the conclusions are presented. Then, the scope of further research pertaining to the arrived conclusions is discussed.

The results presented in the previous chapter demonstrate the capability of an individual absolute quartz-crystal barometer (Intelligent Transmitters Series 6000, manufactured by Paroscientific, Inc.) to detect microbaroms. This is the first time that microbaroms have been detected using single absolute barometers. During calm weather conditions, that is when the wind speed is less than  $0.5 \text{ ms}^{-1}$ , the detection limit of a single barometer has been observed to be about  $0.005 \text{ Pa}$  (50 nanobars), which is about 3 times smaller than that of a single barometer used in [20]. In fact, the observed detection limit was about the same as the detection limit of the array of 28 barometers (Model 216B-250 manufactured by Paroscientific, Inc.) used in [20]. Such a low noise floor allows for the detection of even weak intensity microbaroms by a single barometer, as shown in figure 5.15, provided the wind is not strong.

The time series of bandpass filtered microbaroms and the spectrograms presented in the previous chapter showed the temporal variations of the amplitude and frequency of the microbaroms. The variations in frequency, during significant periods of time, were related to the horizontal wind speed in the lower troposphere. The observed temporal amplitude variations of the microbaroms showed that maximum

intensity microbaroms had been observed close to midnight on some days. Also, there had been a couple of days when the amplitudes were either constantly strong or constantly weak during the entire day. However, these observations did not directly relate to the observations in [12]. Also, there were no observation of microbaroms by any of the barometers (with and without DigiPort) when the wind speed was higher than  $0.5 \text{ ms}^{-1}$ . During such stormy periods, microbaroms could not be observed even in the coherence spectrum between each pair of the barometers. Hence, with these barometers, it is possible to detect microbaroms only during periods when the wind speed is relatively less.

The relative accuracy between the barometers was of the order of a few pascals (few tens of a microbar) with the accuracy being better during moderate and low wind periods. The detection amplitude of the barometer, with a DigiPort connected to it, ranged approximately between 0.05 microbars during calm conditions and 1.0 microbar during stormy conditions, and that of the naked barometer ranged approximately between 0.05 microbars during calm conditions and 0.4 microbars during stormy conditions.

Hence, it can be concluded that these absolute quartz-crystal barometers can be used extensively as an effective and relatively inexpensive method for the detection of microbaroms. Microbarom detection, as mentioned in chapter 1, gives great scope for further research in many fields like hurricane and cyclone tracking [16] and remote sensing of the wind and temperature of the upper atmosphere [12][23]. Also, it was clear that the travel trailer makes the naked barometers less susceptible to wind induced pressure fluctuations than the DigiPort. Considering the fact that microbaroms had been observed only during relatively calm weather conditions and that their RMS amplitudes measured by the three barometers are accurate down to few

tens of nanobars, the choice of using a barometer with DigiPort or a naked barometer inside a relatively large structure (like the trailer or a car) is insignificant for the purpose of detection of microbaroms. There is hope that the distribution of several such barometers to form a three dimensional infrasound network will make microbarom observation possible even during periods of relatively strong winds.

The main requirement for hurricane tracking is the accuracy with which the arrival azimuth of the microbaroms are determined. As a first step towards hurricane or cyclone tracking, an overnight experiment was conducted on 16 Jun, 2009, where in three cars equipped with one of these barometers (without digiport) were stationed all night in the University of Massachusetts Amherst campus. The cars were stationed such that they formed, roughly, an equilateral triangle with 500 m sides. Each car was equipped with a data logger and GPS antenna as well. Since it was a very calm night, the analysis of the data showed good coherence between all the pairs of barometers in the microbarom frequency band confirming the detection of microbaroms. Using the phase spectra between every pair of the barometers and simple geometry, the azimuth angle of arrival of the microbaroms were determined. Preliminary results gave azimuth arrival angles between 75-90 degrees from north (primary source) and between 135-150 degrees (secondary source) from north. These angles of arrival matched closely (within 10 degrees) with the potential generation regions observed from WAVEWATCH III model output provided by National Oceanic and Atmospheric Administration (NOAA). These preliminary results provide a lot of scope for further research in this field.

## BIBLIOGRAPHY

- [1] Arendt, S., and Fritts, D. Acoustic radiation by ocean surface waves. *J. Fluid Mech.* *415* (2000), 1–21.
- [2] Bartlett, M. S. Smoothing periodograms from time series with continuous spectra. *Nature* *161* (1948), 686–687.
- [3] Bedard, A. J. Infrasound originating near mountainous regions in colorado. *J. App. Meteorol.* *17* (1978), 1014–1022.
- [4] Behn, M., Hohreiter, V., and Muschinski, A. A scalable datalogging system with serial interfaces and integrated GPS time stamping. *J. Atmos. Oceanic Technol.* *25* (2008), 1568–1578.
- [5] Benioff, H., and Gutenberg, B. Observations with electromagnetic microbarographs. *Nature* *144* (1939), 478(L).
- [6] Benioff, H., and Gutenberg, B. Waves and currents recorded by electromagnetic barographs. *Bull. Amer. Meteor. Soc.* *20* (1939), 422–426.
- [7] Blackman, R. B., and Tukey, J. W. *The Measurement of Power Spectra*. Dover, New York, 1958.
- [8] Daniels, F. B. Acoustical energy generated by the ocean waves. *J. Acoust. Soc. Am.* *24* (1952), 83.
- [9] Daniels, F. B. Generation of infrasound by ocean waves. *J. Acoust. Soc. Am.* *34* (1962), 352–353.

- [10] Donn, W. L., and Naini, B. Sea wave origin of microbaroms and microseisms. *J. Geophys. Res.* **78** (1973), 4482–4488.
- [11] Donn, W. L., and Posmentier, E. S. Infrasonic waves from the marine storm of April 7, 1966. *J. Geophys. Res.* **72** (1967), 2053–2061.
- [12] Donn, W. L., and Rind, D. Microbaroms and the temperature and wind of the upper atmosphere. *J. Atmos. Sci.* **29** (1972), 152–172.
- [13] Garces, M., Hetzer, C., Merrifield, M., Willis, M., and Aucan, J. Observations of surf infrasound in Hawaii. *Geophys. Res. Lett.* **30**, 24 (2003), 2264.
- [14] Gossard, E., and Munk, W. On gravity waves in the atmosphere. *J. Meteorol.* **11** (1954), 259–269.
- [15] Hagan, M. E., Forbes, J. M., and Richmond, A. Atmospheric Tides. *Encyclopedia of Atmospheric Sciences*. (2003).
- [16] Hetzer, C. H., Waxler, R., Gilbert, K. E., Talmadge, C. L., and Bass, H. E. Infrasound from hurricanes: Dependence on the ambient ocean surface wave field. *Geophys. Res. Lett.* **35** (2008), L14609.
- [17] Kinsler, L. E., Frey, A. R., Coppens, A. B., and Sanders, J. V. *Fundamentals of Acoustics*, fourth ed. John Wiley & Sons, Inc., 1999.
- [18] Mannermaa, J., Kalliomäki, K., Mansten, T., and Turunen, S. Timing performance of various GPS receivers. In *Proc. Joint Meeting of the European Frequency and Time Forum and the IEEE Int. Frequency Control Symp.* (Besancon, France, 1999), IEEE, pp. 287–290.
- [19] Mills, D. L. Internet time synchronization - The network time protocol. *IEEE Trans. on Commun.* **39** (1991), 1482–1493.

- [20] Nishida, K., Fukao, Y., Watada, S., Kobayashi, N., Tahira, M., Suda, N., and Nawa, K. Array observation of background atmospheric waves in the seismic band from 1 mHz to 0.5 Hz. *Geophys. J. Int.* 162 (2005), 824–840.
- [21] Oppenheim, A. V., Schafer, R. W., and Buck, J. R. *Discrete-Time Signal Processing*, 2nd ed. Prentice Hall, Upper Saddle River, New Jersey, 1999.
- [22] Philips, O. M. On the generation of waves by turbulent wind. *J. Fluid. Mech.* 2 (1957), 417.
- [23] Pichon, A. Le, Ceranna, L., Garces, M., Drob, D., and Millet, C. On using infrasound from interacting ocean swells for global continuous measurements of winds and temperature in the stratosphere. *J. Geophys. Res.* 111 (2008), D11106.
- [24] Posmentier, E. S. A theory of microbaroms. *Geophys. J.R. Astron. Soc.* 13 (1967), 487–501.
- [25] Proakis, J. G., and Manolakis, D. G. *Digital Signal Processing: Principles, Algorithms, and Applications*, 4th ed. Pearson Prentice Hall, Upper Saddle River, New Jersey, 2007.
- [26] Schuster, A. On the investigation of hidden periodicities with application to a supposed twenty-six day period of meteorological phenomena. *Terr. Mag.* 3 (1898), 13–41.
- [27] Smith, J. O. *Mathematics of the Discrete Fourier Transform (DFT), with Audio Applications*, 2nd ed. W3K Publishing, 2007.
- [28] Taylor, J. R. *An Introduction to Error Analysis: The Study of Uncertainties in Physical Measurements*, 2nd ed. University Science Books, 1996.

- [29] Welch, P. D. The use of Fast Fourier Transform for the estimation of power spectra: A method based on time averaging over short modified periodograms. *IEEE Trans. Audio and Electroacoustics AU-15* (1967), 70–73.
- [30] Whiteman, C. D., Muschinski, A., Zhong, S., Fritts, D., Hoch, S. W., Hahnberger, M., Yao, W., Hohreiter, V., Behn, M., Cheon, Y., Clements, C. B., Horst, T. W., Brown, W. O. J., and Oncley, S. P. METCRAX 2006: Meteorological Experiments in Arizonas Meteor Crater. *Bull. Amer. Meteor. Soc.* 89 (2008), 1665–1680.
- [31] Willis, M., Garces, M., Hetzer, C., and Businger, S. Infrasonic observations of open ocean swells in the pacific: Deciphering the song of the sea. *Geophys. Res. Lett.* 31 (2004), L19303.